Inorganic Chemistry Laboratory

A Thesis submitted for the degree of Doctor of Philosophy

High Density Ammonia Storage Materials

Author:

David M. Royse

New College

Supervisors:

Prof. W. I. F. David

Prof. P. P. Edwards

Trinity Term 2011

The work described in this Thesis was carried out in the Inorganic Chemistry Laboratory, University of Oxford, from October 2007 until September 2011, under the supervision of Professors William I. F. David and Peter P. Edwards. All of the work is my own unless otherwise stated and has not been submitted previously for any other degree at this or any other university.

David Royse

September 2011

Abstract

David Royse

D. Phil. Thesis

New College, Oxford — Trinity Term 2011

This Thesis considers the use of solid-state metal ammines as ammonia storage materials and endeavours to understand these materials on a fundamental chemical level. The ammines of $LiBH_4$, $MgCl_2$, $MgBr_2$, MgI_2 and $Mg(BH_4)_2$, are investigated. The structures of lithium borohydride ammines, $Li(NH_3)_nBH_4$ with $n \in \{1, 2, 3, 4\}$, are solved using X-ray and neutron diffraction, vibrational spectroscopy, nuclear magnetic resonance, and first-principles calculations. The reversibility, bonding and ammonia storage properties of this system are discussed, and investigated using gravimetric analysis and vibrational spectroscopy. The ammines of magnesium halides are investigated using X-ray and neutron powder diffraction, gravimetric techniques, nuclear magnetic resonance, first-principles calculations and vibrational spectroscopy. Their disordered structures, bonding, and decomposition are discussed, and the trends in their properties are used to interpret the properties of other ammines. The ammines of magnesium borohydride are investigated using X-ray and neutron powder diffraction, gravimetric techniques, first-principles calculations and vibrational spectroscopy. The structure, decomposition and reversibility of $Mg(NH_3)_6(BH_4)_2$ as an ammonia store are presented. Throughout the Thesis and at the end of each Chapter the possibility of using these ammines as solid-state ammonia stores is discussed.

Acknowledgements

Many people have helped and supported me over the course of this research and to all of them I am grateful, it has been a privilege to work with so many intelligent and knowledgeable people.

Firstly thanks must go to Prof. Peter Edwards for giving me the opportunity to work on this project in such a fascinating area of research.

I would like to thank Prof. Bill David for his supervision and seemingly unbounded knowledge of crystallography the universe and everything and for spending the time proof-reading this work. Also Dr Martin Jones who has been a constant source of guidance and advice.

The various post-docs who have helped and advised me along the way: Dr Simon Johnson for showing me the experimental ropes all those years ago and for his unnatural interest in ammonia. Dr Marco "Prince of the Beam" Sommariva in particular for his heroic efforts on beam times and mastery of the IGA^{n}. Dr Sam Callear for help in taming a master-less IGA^{n} post-Marco and for remaining a voice of reason and crystallography. Dr Matt Lodge for always being willing to lend advice on all things experimental and ammonia. Dr Timmy Ramirez-Cuesta for his help and patience in analysis of INS data. Thanks must also go to others who have helped with data analysis and as instrument scientists in Oxford, ISIS, RAL and the ESRF; Dr Francesca Fabbiani, Dr Amber Thompson, Dr David Apperley, Prof. Andy Fitch, Dr Kevin Knight, Dr Aziz Daoud-Aladine, and Dr Nick Rees.

To all those who I have shared an office with for keeping me entertained, always being ready with an answer or opinion, and for cake Fridays. In particular; Chris, Anne, Kate, Philippe and Andrew. Particular thanks must go to Philippe for his assistance with Castep.

To the boys and girls, all the gang, from Fairacres and Weston for making this DPhil about far more than just chemistry. Especially for every BBQ Tuesday, climbing and the gift of endurance sport! Special mention must go to Matt for his enthusiasm in trying teaching me Python and Ruby, and to Ed for giving me some useful research ideas.

I would also like to thank my parents for their love and unwavering support throughout these last 21 (?!) years of education.

Last but not least to Nikki for her friendship and support throughout.

Contents

List of Figures

Chapter 1

Introduction

This Thesis considers the use of solid-state metal ammines as ammonia storage materials and endeavours to understand these materials on a fundamental chemical level. This Chapter contains an overview of the need for, and the requirements of, ammonia storage materials. A background to the materials investigated in later Chapters is discussed, as well as other important concepts and the aims of the Thesis.

1.1 The Widespread Use of Ammonia

Ammonia is one of the most abundantly produced inorganic chemicals in the world. Of the 124,000,000 t produced annually,[1] around 85 % is used as fertiliser either by direct application or in ammonium nitrate which is produced as shown in Equation 1.1. One of the most important reactions involving ammonia is the Ostwald process that is shown in Reaction 1.2, and is used to produce nitric acid. This acid is hugely important to the chemical industry, finding uses in the production of; plastics, fibres, resins, explosives, dyes and pharmaceuticals. Ammonia itself is also used as an industrial scrubber to remove SO_2 from flue gas, and as a refrigerant.[2–5]

$$\mathrm{HNO_{3\,(aq)}} + \mathrm{NH_{3\,(g)}} \longrightarrow \mathrm{NH_4NO_{3\,(aq)}} \tag{1.1}$$

$$4\,\mathrm{NH_{3\,(g)}} + 5\,\mathrm{O_{2\,(g)}} \longrightarrow 4\,\mathrm{NO_{(g)}} + 6\,\mathrm{H_2O_{(g} \tag{1.2}$$

$$2\,\mathrm{NO_{(g)}} + \mathrm{O_{2\,(g)}} \longrightarrow 2\,\mathrm{NO_{2\,(g)}}$$

$$3\,\mathrm{NO_{2\,(g)}} + \mathrm{H_2O_{(l)}} \longrightarrow 2\,\mathrm{HNO_{3\,(aq)}} + \mathrm{NO_{(g)}}$$

Alongside its already widespread uses, there are a number of emerging and potentially important uses for ammonia. When used as a fuel, pressurised ammonia has the lowest cost in terms of $\$\mathrm{GJ}^{-1}$ compared to gasoline, LPG, methanol and hydrogen.[6] Its potential energy may be released either by direct combustion or in a solid-oxide fuel cell.[7–9] With a high hydrogen content of 17.6 wt% it has been speculated that, with catalytic cracking on the point of demand, ammonia may be a suitable energy vector in a hypothetical hydrogen economy. The already well-established production facilities, distribution network and simple handling procedures would help ease the transition to such an economy.[10–14] Although the potential use of ammonia as a fuel attracts major research interest, there are other emerging uses. One of the more interesting of these, that requires an effective on-board store of anhydrous ammonia, is selective catalytic reduction (SCR).[15,16] This process may be used to remove harmful NO_x gases from diesel exhaust fumes as shown in Reaction 1.3.

$$\mathrm{NO_{(g)}} + \mathrm{NO_{2\,(g)}} + 2\,\mathrm{NH_{3\,(g)}} \longrightarrow 2\,\mathrm{N_{2\,(g)}} + 3\,\mathrm{H_2O_{(g)}} \tag{1.3}$$

1.2 Properties of Ammonia and Gas Storage

The physical properties of ammonia have helped enable its widespread use; it is essentially non-flammable, and can be easily handled as a liquid in simple vessels

thus negating the need for expensive pressure vessels or refrigeration techniques required for handling other gases. However, it possesses a number of drawbacks, primarily its toxicity but significantly it is a corrosive gas with a high coefficient of thermal expansion and high vapour pressure at ambient conditions. Currently ammonia is stored or transported in aqueous solution, as a gas (but one that will be a liquid when stored at a pressure of greater than 7 bar), or as a refrigerated liquid at -33 °C. The densities of stored ammonia vary from 0.73 gL^{-1} for gaseous ammonia at 1 atm and 15 °C to 682 gL^{-1} for liquid ammonia at -33 °C. Consideration of thermal expansion means that ammonia storage tanks have a practical usable capacity of only 85 %.[13,17]

1.2.1 Solid State Ammonia Stores

Solid state ammonia stores, and in particular metal ammines, have been proposed as a useful method to store ammonia. Specific uses for such systems include; *i*) indirect hydrogen storage;[18] *ii*) refrigeration;[19] and *iii*) separation and storage during ammonia synthesis.[20,21] These, and other, solid state methods may allow improvements in ammonia storage that include:

1. Reduction or control of vapour pressure.

2. Improving safety to minimise the amount of toxic ammonia release if the storage vessel were to break.

3. Increasing the storage density of the system.

4. Increasing the thermal stability of the storage medium with respect to thermal expansion.

5. Providing storage methods specific to novel uses for example on-board SCR or hydrogen storage.

It is the group II halides that have received particular attention, with different compounds favoured for different uses. For indirect hydrogen storage and on-board SCR, $Mg(NH_3)_6Cl_2$ is favoured because of its high ammonia density and low vapour pressure.[16,18] For separating ammonia from other gases, $Ca(NH_3)_8Cl_2$ or $Ca(NH_3)_8Br_2$ have been chosen as, along with a high ammonia density, it is possible to cycle ammonia in and out of these compounds using the pressure swing absorption method.[22]

Any material that is to be used for gas storage must also consider the following criteria that are well documented in the hydrogen storage literature but adapted here to provide general guidelines for the requirements of ammonia storage systems:[23]

1. The gas must be stored safely and the system must conform to appropriate standards.

2. The cost must be comparable to existing storage options or present significant system advantages.

3. There must be a high ammonia capacity.

4. The system must allow for controlled ammonia release.

5. The energy penalty for storage and release must be reasonable, especially if the gas is to be used as a fuel.

6. The system must be an improvement on existing options.

1.3 Thermodynamic Considerations

These ammine systems can be described as the reaction between a solid and ammonia as shown in Reaction 1.4. In this case, the relationship between temperature and pressure may be described by the Clausius-Clapeyron equation (Equation 1.5).

Although this relationship is normally only applied to the transformation of a single phase, if it is considered that the contribution of M remains constant then the reaction simply involves the vaporisation of NH_3 in a specific environment. Following the standard derivation available in many texts, the integrated form of the Clausius-Clapeyron equation, that describes the transition from solid to gas, as shown in Equation 1.6, is obtained.[24] From this it is clear that in order to reduce the vapour pressure of a sample, the desorption temperature must increase. Thus balancing these two factors is the essence of producing an effective solid state ammonia store.

$$\mathrm{M(NH_3)_{n(s)} \rightleftharpoons M_{(s)} + nNH_{3\,(g)}} \tag{1.4}$$

$$\frac{dp}{T} = \frac{\Delta H}{T\Delta V} \tag{1.5}$$

$$\frac{\ln p_1}{\ln p_2} = \frac{\Delta H_{vap}}{R}\left(\frac{1}{T_1} - \frac{1}{T_2}\right) \tag{1.6}$$

1.4 Magnesium Halide Ammines ($Mg(NH_3)_nX_2$)

As mentioned above, recent attention has focussed on utilising $Mg(NH_3)_6Cl_2$ as an ammonia storage material. Particularly important work by Liu et al. considers the temperature swing absorption method suitable for ammonia storage in $MgCl_2$,[20] while Christensen et al. have contributed many publications following their introduction of $Mg(NH_3)_6Cl_2$ as a potential hydrogen storage material.[18]

The $MgCl_2$ system has been well characterised with the most notable studies reporting; *i*) the enthalpies of desorption;[25] *ii*) formation of an expanded structure on desorption that allows for fast reaction kinetics;[26] *iii*) a calculated desorption mechanism that supports the observation of an expanded structure;[27] and *iv*) a detailed

account of a model reactor that shows $Mg(NH_3)_6Cl_2$ would be a suitable material to use for SCR.[16] Despite this wealth of reported knowledge, data considering the rest of the halide series are scarce. In one report, Sørensen et al. gather the desorption enthalpies of 90 metal halide ammines that include $MgBr_2$ and MgI_2 though their sources are not clear.[27]

The work of Christensen et al. shows the clear potential for the use of $Mg(NH_3)_6Cl_2$ as an ammonia storage material with a high capacity of 52 wt%. Indeed to this end, the system is well characterised, but on a fundamental level there are still areas where an increased understanding of these materials would be useful. In particular, understanding the properties of the group and how the anion affects properties is important in order to develop ammonia storage materials.

1.4.1 Ammonia Sorption Pathways

The existence of magnesium halides $Mg(NH_3)_nX_2$ (for X = Cl, Br and I) with $n \in \{1, 2, 6\}$ for X = Cl, Br and $n \in \{2, 6\}$ for X = I, was first shown by Biltz and Hüttig, who in 1921 measured the vapour pressure of NH_3 over magnesium halides as a function of temperature.[28] The majority of reports on $Mg(NH_3)_6Cl_2$ agree that ammonia desorption is reversible and occurs via the n = 6, 2, 1, 0 pathway as shown in Reaction 1.7.[16,18,25] An alternative report suggests that desorption occurs via the n = 6, 4, 2, 0 pathway that is shown in Reaction 1.8.[29] The different experimental conditions may account for the observed differences in sorption pathways. Zhu et al. argue that carrying out thermogravimetric analysis under nitrogen on the milligram scale means that the negligible ammonia pressure promotes the alternative desorption pathway. While the majority pathway is observed by; Elmøe et al. who use a higher ammonia pressure in a demo SCR reactor to control ammonia desorption, Christensen et al. who used a similar non-negligible ammonia pressure, and Liu et al. who observed the n = 6, 2 and 1 phases using adsorption isotherm measurements

in a similar manner to Biltz and Hüttig.

$$\mathrm{Mg(NH_3)_6Cl_2} \rightleftharpoons \mathrm{Mg(NH_3)_2Cl_2} + 4\,\mathrm{NH_3} \tag{1.7}$$

$$\mathrm{Mg(NH_3)_2Cl_2} \rightleftharpoons \mathrm{Mg(NH_3)Cl_2} + \mathrm{NH_3}$$

$$\mathrm{Mg(NH_3)Cl_2} \rightleftharpoons \mathrm{MgCl_2} + \mathrm{NH_3}$$

$$\mathrm{Mg(NH_3)_6Cl_2} \rightleftharpoons \mathrm{Mg(NH_3)_4Cl_2} + 2\,\mathrm{NH_3} \tag{1.8}$$

$$\mathrm{Mg(NH_3)_4Cl_2} \rightleftharpoons \mathrm{Mg(NH_3)_2Cl_2} + 2\,\mathrm{NH_3}$$

$$\mathrm{Mg(NH_3)_2Cl_2} \rightleftharpoons \mathrm{MgCl_2} + 2\,\mathrm{NH_3}$$

1.4.2 Magnesium Hexa-ammine Crystal Structure and Disorder

In 1965, Olovsson referred to earlier work by Wyckoff and stated that all the $\mathrm{Mg(NH_3)_6X_2}$ compounds have the same $\mathrm{K_2PtCl_6}$ structure.[30,31] This may be thought of as the fluorite structure with $\mathrm{M(NH_3)_6^{2+}}$ in the $\mathrm{Ca^{2+}}$ sites and $\mathrm{X^-}$ in the $\mathrm{F^-}$ sites and is shown in Figure 1.1.[32] It was not until 2000 that any detailed structural information of $\mathrm{Mg(NH_3)_6Cl_2}$ was published by Hwang et al. confirming the $\mathrm{K_2PtCl_6}$ structure with a cubic unit cell parameter of a = 10.1899(4) Å and Mg−N bond length of 2.197(3) Å, though they do not provide any information on hydrogen positions.[33] In contrast to the data available on $\mathrm{Mg(NH_3)_6Cl_2}$, there are far fewer published works on either $\mathrm{Mg(NH_3)_6Br_2}$ or $\mathrm{Mg(NH_3)_6I_2}$. A structural analysis of $\mathrm{Mg(NH_3)_6Br_2}$ has been performed in the PhD Thesis of M. W. Friedriszik although these data are not freely available.[34]

The $\mathrm{Mg(NH_3)_6X_2}$ structure belongs to the $Fm\bar{3}m$ space group in which the $\mathrm{NH_3}$ molecule sits on a site with 4-fold rotational symmetry. The C_{3v} symmetry of the ammonia molecule either means that there is disorder in the hydrogen atom

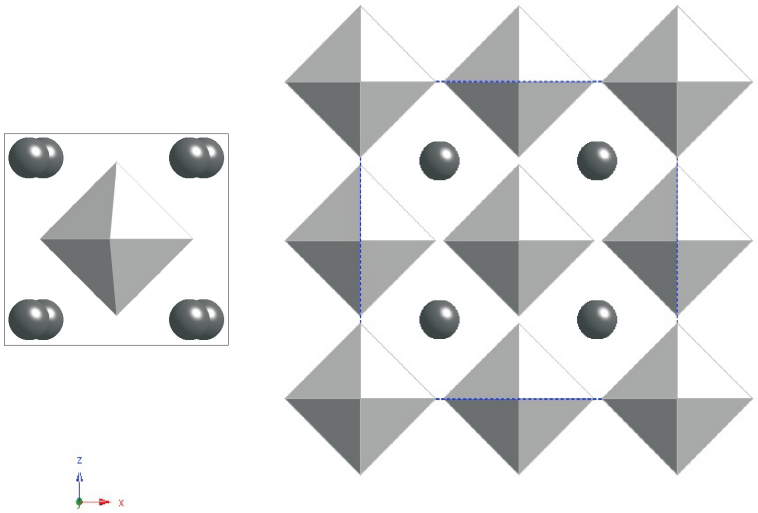

Figure 1.1: The K_2PtCl_6 structure showing $PtCl_6^{2-}$ octahedra and K^+ atoms in light and dark grey respectively. The local coordination of a single $PtCl_6^{2-}$ octahedron is shown in the inset on the left hand side.

positions about the nitrogen atom or that the space group assignment is incorrect. This type of disorder has been recognised, if not completely understood, for many years.[35,36] Indeed in some of the earliest work on the isostructural $Ni(NH_3)_6X_2$, Wyckoff acknowledges that placing the nitrogen atom on the 24(a) cubic site in $Fm\bar{3}$, $F432$ or $Fm\bar{3}m$ would mean that "two of the hydrogen atoms of the ammonia in this compound are different from the third" but that "this is so contrary to what would have been expected from chemical considerations that in the absence of any satisfactory crystallographic determination of its class of symmetry, it is more natural to assign this salt to the space-group [with lower symmetry]." A number of studies of $M(NH_3)_6X_2$ (M = V, Cr, Fe, Mn, Ni, Co and X = Cl, Br, I) suggest that the electron density of the hydrogen atoms is located around four maxima that align the N−H bonds in the direction of X^-.[37–41] Such detailed information was not reported for the magnesium halides until 2011 when Sørby et al. published a combined neutron diffraction and molecular dynamics study of $Mg(ND_3)_6Cl_2$.[42] They proposed 2 hydrogen sites; 96k and 96j with occupancies of 1/2 and 1/4

respectively, a model exactly in line with Wyckoff's predictions some 89 years earlier!

1.4.3 Magnesium Diammine Crystal Structure and Disorder

Leineweber et al. have published the structures of $Mg(NH_3)_2Cl_2$, $Mg(NH_3)_2Br_2$ and $Mg(NH_3)_2I_2$, concluding that all three compounds have the same local structure consisting of chains of edge sharing $MgX_4(NH_3)_2$ octahedra. The packing of these chains is such that each ammonia molecule has four nearest-neighbour halide ions, but the overall packing pattern varies from the chloride to the identical bromide and iodide, as shown in Figure 1.2. In both cases disorder is observed in the hydrogen sites, with four-fold disorder and alignment of the N−H bonds in the direction of X^- once again favoured.[34]

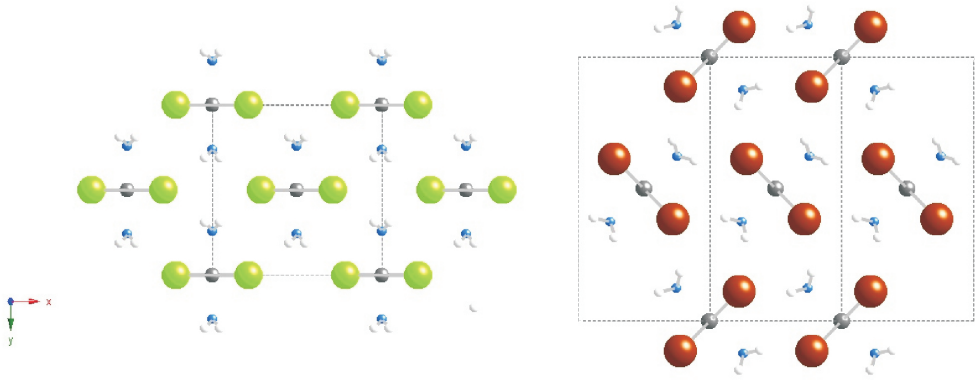

Figure 1.2: A comparison of the structures of $Mg(NH_3)_2Cl_2$ and $Mg(NH_3)_2Br_2$, both viewed along the z-axis. Mg is shown in grey, N in blue, H in off-white, Cl in lime green and Br in red-brown.

1.4.4 Low-temperature Ordered Crystal Structure

Given the room temperature disorder, it is anticipated that the ammonia molecules in $Mg(NH_3)_6X_2$ order at low temperatures. The very similar and isostructural compound $Ni(NH_3)_6Cl_2$ has been studied at low temperatures (due largely to its magnetic properties) but no experimental work has been performed on $Mg(NH_3)_6Cl_2$.

Eckert et al. reported that $Ni(NH_3)_6Cl_2$ orders to form a structure that is in a subgroup of space group $R\bar{3}$ at 27 K,[43] but no further structural solution has been published. A first-principles study of $Mg(NH_3)_6Cl_2$ was reported by Tekin et al., based on the assumption that $N{-}H^{\delta+}\cdots Cl^-$ interactions would stabilise an ordered structure they performed search algorithms to maximise the number of these interactions within potential structures.[44] The focus of this work was not on the crystal structure but they reported 4 possible space groups $R\bar{3}$, $I4/m$, $C2/m$ and $Cmmm$ with no atomic coordinates presented for the potential structures.

The chloride and bromide diammines have been well characterised in a comprehensive study by Leineweber et al. that reports low temperature ordering of ND_3, and discusses the more subtle presence of order-disorder phase transitions.[45]

1.5 Magnesium Borohydride Ammines ($Mg(NH_3)_n(BH_4)_2$)

The borohydride compound $Mg(NH_3)_6(BH_4)_2$ has been know for over 50 years, with early research interest driven by its high hydrogen content and explosive potential.[46,47] A number of Russian scientists carried out research on this and other borohydrides, Semenenko et al. confirmed by IR spectroscopy that $Mg(NH_3)_6Cl_2$ was "salt-like" and comprised of $Mg(NH_3)_6^{2+}$ and BH_4^- ions. Their samples were synthesised in the simplest reported way by the metathesis shown in Reaction 1.9 with subsequent exposure of the etherate to ammonia as shown in Reaction 1.10. They reported that the solid crystallises in an orthorhombic unit cell though did not suggest a possible structure.[48] The synthesis of an isolated di- and tri-ammine by reaction of magnesium borohydride in benzene and ether has also been reported,[49] though has not been repeated.

$$MgCl_2 + NaBH_4 \xrightarrow{Et_2O} Mg(Et_2O)_2(BH_4)_2 + NaCl \tag{1.9}$$

$$Mg(Et_2O)_2(BH_4)_2 + (ex)NH_{3\,(g)} \longrightarrow Mg(NH_3)_6(BH_4)_2 + 2\,Et_2O \tag{1.10}$$

Until recently, the most complete study of decomposition pathways was reported by Konoplev et al. who observed that decomposition of the hexa-ammine occurs in two steps releasing ammonia and then hydrogen as shown in Reaction 1.11. The existence of the hexa- and di-ammine were characterised by infra red spectroscopy.[50]

$$Mg(NH_3)_6(BH_4)_2 \xrightarrow[100\ ^\circ C,\ 7\ h]{in\ vacuo,\ -4\,NH_3} Mg(NH_3)_2(BH_4)_2 \tag{1.11}$$

$$Mg(NH_3)_2(BH_4)_2 \xrightarrow[170\text{-}240\ ^\circ C]{in\ vacuo} Mg + 2\,BN + 5\,H_2$$

Research efforts have returned to these ammines, once again motivated by the high hydrogen content, though this time for slightly different reasons. A comprehensive study by Soloveichik et al. focused on the synthesis and decomposition of $Mg(NH_3)_2(BH_4)_2$ as a potential hydrogen storage material. Observing that $Mg(NH_3)_2(BH_4)_2$ releases hydrogen at 120 °C, a temperature that is significantly lower than its parent $Mg(BH_4)_2$ at 323 °C. They propose that complete decomposition of $Mg(NH_3)_2(BH_4)_2$ occurs in a two steps beginning at 120 °C and 220 °C with the overall irreversible reaction shown in Reaction 1.12. They also suggest that $Mg(NH_3)_6(BH_4)_2$ has the K_2PtCl_6 structure with a cubic unit cell parameter of a = 10.82(1) Å, but do not provide any atomic positions.[51]

$$3\,Mg(NH_3)_2(BH_4)_2 \xrightarrow{120\text{-}500\ ^\circ C} Mg_3B_2N_4 + 2\,BN + 2\,B + 21\,H_2 \tag{1.12}$$

The reported crystal structure of $Mg(NH_3)_2(BH_4)_2$ is unusual; unlike the hexa-ammine, it is essentially molecular. Each Mg^{2+} cation is coordinated by two BH_4^- anions and two NH_3 molecules, these molecules pack together in a structure that appears to be stabilised by $N{-}H^{\delta+}\cdots{}^{\delta-}H{-}B$ dihydrogen bonds that are discussed further in Section 1.7. It is thought that this dihydrogen bonding promotes hydrogen

release at a lower temperatures in $Mg(NH_3)_2(BH_4)_2$ compared to $Mg(BH_4)_2$.[51]

Although the magnesium borohydride hexa-ammine has an ammonia content of 65 wt%, the decomposition from the diammine is irreversible. Assuming that the loss of the first for ammonia molecules is reversible, this leaves a usable ammonia storage content of 44 wt% that is released at around 100 °C.

1.6 Lithium Borohydride Ammines ($Li(NH_3)_nBH_4$)

The study of coordination compounds formed between lithium borohydride and ammonia at room temperature dates back to the discovery of borohydrides and the work of Hunt and Cowie in 1955.[52] However, the first and only comprehensive studies of pressure-composition-temperature relationships and densities of these systems were performed by Sullivan and Johnson in 1959.[53] They reported that lithium borohydride forms ammines of the composition $Li(NH_3)_nBH_4$, with $n \in \{1, 2, 3, 4\}$. Thermolysis of the ammines was reported to proceed primarily through the stepwise loss of ammonia, as shown in Reaction 1.13, though a competing alternative reaction shown in Reaction 1.14 was also observed to a lesser extent.

$$Li(NH_3)_nBH_{4\,(s)} \rightleftharpoons Li(NH_3)_{n-m}BH_{4\,(s)} + mNH_{3\,(g)} \tag{1.13}$$

$$Li(NH_3)BH_{4\,(s)} \longrightarrow LiNH_2BH_{3\,(s)} + H_{2\,(g)} \tag{1.14}$$

The summary of their report in the form of a phase diagram is shown in Figure 1.3. In the diagram, the regions v, w, x and y represent the equilibrium between solid and gaseous phases as shown in Reaction 1.13 suggesting that these reactions should be observed below 15 °C. The diagram is however complex with each of the regions a to j involving a solid-liquid equilibrium. By plotting the equilibrium

pressure of the mole ratios of $NH_3/LiBH_4$ given by Sullivan and Johnson, it is in principle possible to extract the vapour pressures at one of the given temperatures for each of the phases and these data are given in Appendix B. This is the source of the estimated vapour pressure for $Li(NH_3)BH_4$ given below. There is however, a significant degree of uncertainty in the data and thus there is limited value in full analysis.

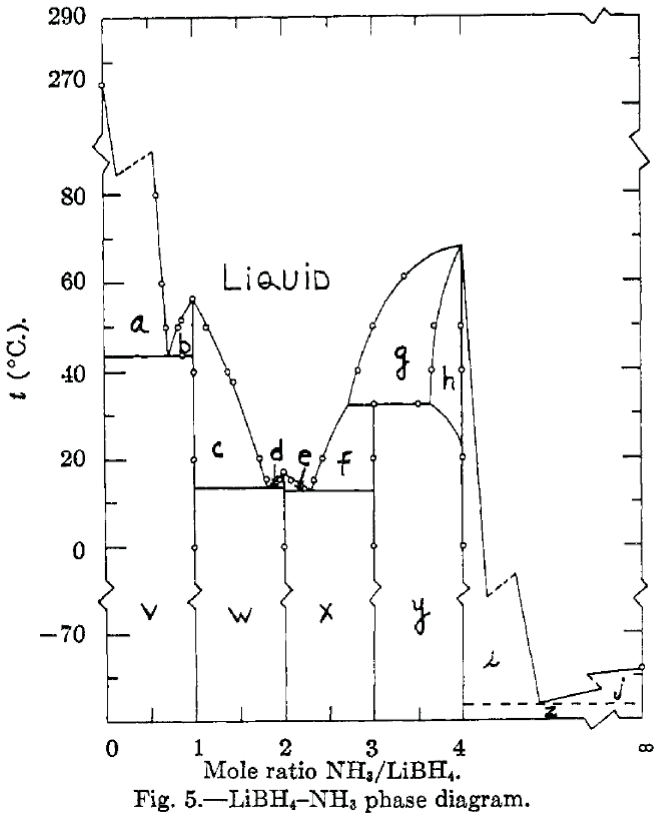

Fig. 5.—$LiBH_4$–NH_3 phase diagram.

Figure 1.3: A phase diagram for $Li(NH_3)_nBH_4$ produced by Sullivan and Johnson

Assuming that the progress of Reaction 1.14 is negligible, then these ammines have a reversible ammonia storage content of *ca.* 44, 61, 70 and 76 wt% for $n = 1, 2, 3$ and 4 respectively. The monoammine, $Li(NH_3)BH_4$, has the lowest ammonia content (*ca.* 44 wt%), but has the advantage of the lowest vapour pressure that is between 2.1 mbar and 10 mbar at 20 °C.

1.7 Hydrogen and Dihydrogen Bonding

In systems that contain ammonia and halide anions, there is a clear possibility that hydrogen bonds exists (where the definition of hydrogen bonding used in this Thesis is most generally described as "a hydrogen atom bonded to two or more other atoms."[54]) This can be thought of as the interaction of a lone pair, and typically the occupied p-orbitals of N, O or F, with the unoccupied σ^* orbital of an A−H bond. In the case of the borohydride ammines, a different type of hydrogen bond may exist, that is a dihydrogen bond between N−$H^{\delta+}$ and $H^{\delta-}$−B. Formally this interaction is described as the interaction between "σ-bonding electron pairs of M−H bonds and traditional X−H proton donors." These may be identified by short H···H interactions less than the Van der Waals radii of two hydrogen atoms at 2.4 Å, but are considered significant when the H···H distances are between 1.2 Å and 2.2 Å; the shorter the distance, the stronger the bond. A second indicator of dihydrogen bonding is a strongly bent XH···H−M angle between 90 ° and 135 °. A significant feature of these bonds is the ability to exchange weak H···H interactions with strong covalent ones, facilitating the release of H_2.[55,56]

1.8 Aims of this Thesis

This Thesis aims to synthesise and characterise materials with potential use as general purpose ammonia stores. The focus will therefore be on lowering the vapour pressure and desorption temperature of metal ammines whilst attempting to increase the gravimetric ammonia density. In fully characterising $Mg(NH_3)_6X_2$ with X = Cl, Br, I and BH_4 and $Li(NH_3)_nBH_4$ both structurally and chemically it is hoped that the properties of these systems may be explained, enabling a greater understanding, and ultimately development of, materials for use in ammonia storage.

Chapter 2

Experimental Methods

This chapter covers all the experimental methods used within this Thesis. In the first section, practical synthetic methods are discussed. In the second section, analytical methods are described along with a brief description of the theory behind the methods.

Synthetic Methods

2.1 Storage and Handling

The vast majority of starting materials used in this Thesis were air- or moisture-sensitive, therefore all preparation and storage took place under an inert atmosphere inside an argon atmosphere glovebox. Levels of O_2 and H_2O were kept at less than 0.1 ppm by continually circulating the gas within the glovebox through columns containing molecular sieves and phosphoric acid. All glassware was dried and ports were pump-purged before use.

2.2 Sources and Purities of Starting Materials

All starting materials were anhydrous and where possible were used without further preparation. $MgCl_2$ (Aldrich, 99.99 %), $MgBr_2$ (Aldrich, 99.995 %), MgI_2 (Aldrich, 99.998 %), $LiBH_4$ (Aldrich, $\geq$ 99.99%), $Mg(BH_4)_2$ (Aldrich, 95 %), NH_3 (BOC Special Gases, 99.98 %), ND_3 (BOC Special Gases and CK Gases, 99.99 %), ^{11}B (Alfa Aesar, 99.9 %), Li (Aldrich, 99.95 %), Na (Aldrich, 99.95 %), D_2 (CK Gases, 99.8 %). Sodium metal was purchased in mineral oil and washed with pentane on a Schlenk line under nitrogen gas before further use.

2.3 High Pressure Furnace

Isotopically enriched (^{11}B and D) lithium and sodium borodeuteride samples were produced using a Parr Series 4740 High Pressure Vessel capable of withstanding a pressure of 200 bar at 700 °C. The instrument consists of a 75 cm^3 stainless steel reactor, sealed with a steel alloy screw cap on a graphite gasket. A rigid mantle heater and temperature controller were used to control the temperature. The development of the method and the equipment is based on that of Friedrichs et al. and reported in the D. Phil. Thesis of Dr. Anne Nickels.[57,58]

The solid elements were used in the proportions given in in Table 2.1 and were loaded into the reactor vessel inside the glovebox described in Section 2.1. The reactor vessel was then sealed and transferred to the furnace, where it was evacuated to a pressure of approximately 1×10^{-2} mbar. Following evacuation, the reactor was charged with deuterium gas to a pressure of 55 bar (an equivalent of 183 bar at 700 °C assuming a perfect gas) and then sealed. Reactions were heated to 700 °C for 12 hours; the reactor was then allowed to cool and finally re-pressurised to 55 bar and heated to 700 °C for a further 12 hours. Yields were generally poor and a significant quantity of the metal deuterides (LiD or NaD) were generated as by-products.

Table 2.1: Amounts of reactants used in high pressure synthesis of $Li^{11}BD_4$ and $Na^{11}BD_4$

Compound	Amount of Li or Na		Amount of ^{11}B		Amount of D_2
	g	$gmol^{-1}$	g	$gmol^{-1}$	$gmol^{-1}$
$Li^{11}BD_4$	0.6	0.086	0.8	0.073	0.17
$Na^{11}BD_4$	2.0	0.087	0.8	0.073	0.17

2.4 Schlenk Line Synthesis and Purification

Standard Schlenk line techniques were employed for solution based synthesis of magnesium borohydride and washing of lithium and sodium borodeuteride following high pressure furnace synthesis.[59] All solvents were dried by standard methods and distilled before use.

Magnesium borohydride ($Mg(BH_4)_2$) and the isotopically enriched (^{11}B and D) magnesium borodeuteride ($Mg(^{11}BD_4)_2$) were synthesised using the solution based metathesis reaction between $MgCl_2$ and $NaBH_4$ (or $Na^{11}BD_4$) in diethyl ether (Et_2O). Reactants were ground together in a 1:2.2 molar ratio and refluxed in Et_2O for a period of 120 hours at 60 °C. The solvent was topped up at regular intervals when the level was observed to have dropped significantly. The reaction was filtered and a soluble product, $Mg(Et_2O)_2(BH_4)_2$, was obtained by drying under vacuum at ca. 50 °C; desolvation of this etherate was achieved on exposure to ammonia gas.

Isotopically enriched (^{11}B and D) sodium borodeuteride was washed in di-isopropyl amine ($(i{-}Pr)_2NH$) before use in any reactions; the mixture was stirred vigorously for a period of 2 hours and then allowed to settle overnight. The soluble product was then separated from the insoluble impurities and dried under vacuum at 40-45 °C for 2 hours. Isotopically enriched lithium borodeuteride ($Li^{11}BD_4$) was washed using the same technique, but using diethyl ether as the solvent.

2.5 Synthesis of Ammines

Syntheses involving ammonia were undertaken using a custom made glass gas handling (ammonia) line, a schematic of which is shown in Figure 2.1. All recorded gas pressures were read from the fitted pressure and vacuum gauges; the gas regulators were not used for these measurements. The maximum operating gas pressure was limited to 1500 mbar, with a minimum pressure of 1×10^{-3} mbar reached during evacuation.

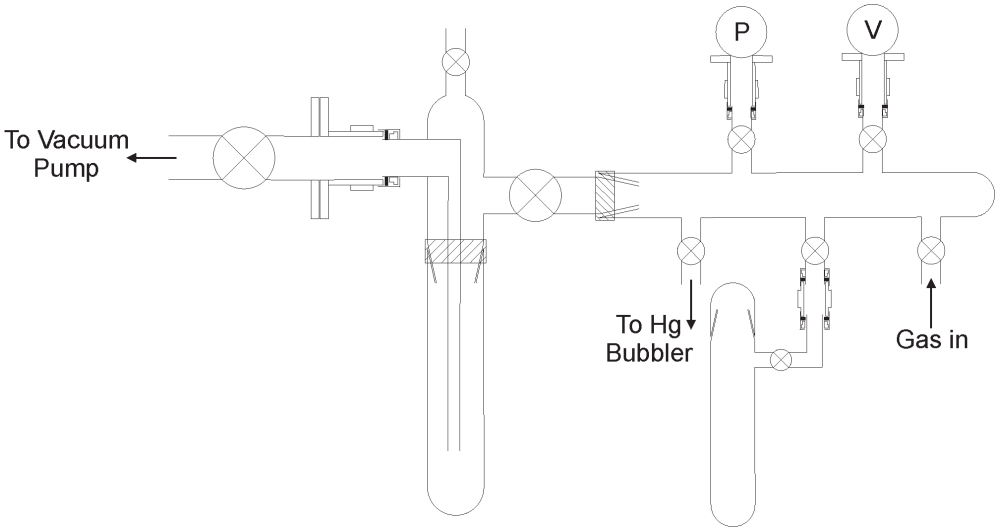

Figure 2.1: A schematic diagram of the gas line used for synthesis of ammines

Before addition of ammonia, sealed Schlenk tubes containing reactants were evacuated for a period of hours. Ammonia was slowly introduced to the system via the standard ammonia regulator until a final pressure of ca. 1000 mbar was reached. The pressure was maintained at ca. 1000 mbar for a period of several hours in an otherwise fixed system. Following exposure to ammonia, the Schlenk tube was once more evacuated and transferred to the argon atmosphere glovebox.

Single crystals of $Li(NH_3)BH_4$ were grown using the experimental set up shown in Figure 2.2. Samples were exposed to flowing ammonia gas, until no further volume expansion nor evolution of heat was observed. The gas supply was then switched from ammonia to argon. The sample remained under flowing argon for a period of

12 hours, before being transferred to the argon atmosphere glovebox.

Figure 2.2: The apparatus used for single crystal growth, showing a reaction between $LiBH_4$ and NH_3

Analytical Techniques

2.6 Diffraction Techniques[60]

Diffraction techniques are based on the elastic scattering of waves from structures that have long range order. In crystalline materials where the atoms are arranged in an ordered periodic array and are of the order of a few Ångstroms apart, diffraction of X-rays, neutrons and electrons of appropriate energies occurs. Diffraction techniques are routinely used in *i*) comparison of a diffraction pattern to a known database in order to identify phase composition; *ii*) analysis of phase purity; *iii*) crystal structure determination; *iv*) identification of phase transitions; and *v*) extraction of subtle

structural aspects, including particle size and strain, and atomic disorder.

When radiation interacts with atoms, it is scattered in all directions and constructive interference only occurs in a limited number of well-defined angles. Careful analysis of the position and intensity of these diffracted beams means that the position and chemical nature of the atoms within the crystal may be deduced. The first step in analysing diffraction data is to determine the size of the unit cell. When a beam of radiation interacts with a set of planes in a crystal, defined by the Miller indices (hkl), diffraction occurs when the geometry of the situation fulfils Bragg's Law:

$$\lambda = 2d_{hkl} \sin\theta$$

where λ is the wavelength of the radiation, d_{hkl} is the perpendicular separation of the (hkl) planes and θ is half of the diffraction angle, 2θ. There are an infinite number of (hkl) planes within a crystal or crystallite, but they will only diffract the incoming beam if they are at the appropriate angle. The complete diffraction pattern is one in which all possible angles are observed with equal (or normalised) incident radiation, application of Bragg's law to the peak positions in the diffraction pattern produces a list of d_{hkl} values for the compound. Assigning (hkl) values to these is the process of indexing the pattern, and is used to determine the unit cell size and type.

The intensities of the diffracted beams are dependant on a number of factors (the relevance of which depends largely on how carefully diffraction data are being analysed) they are:

1. the type of radiation
2. the Bragg angle (θ) of the diffracted beam
3. the scattering power of the atoms present (the atomic scattering factor, f)

4. the arrangement of atoms in the crystal (the structure factor, F)
5. the thermal vibrations of the atoms (the temperature factor. B or W)
6. the dimensions, shape and perfection of the crystal or crystallites (the form factor)
7. the number of equivalent (hkl) planes present (the multiplicity) (in powder diffraction but not single crystal)

These relationships are summarised as

$$I_{hkl} \propto (Lp)_{hkl} J_{hkl} F_{hkl}^2 e^{-2W_{hkl}} A_{hkl} \tag{2.1}$$

where $(Lp)_{hkl}$ is the Lorentz polarization factor, J_{hkl} is the multiplicity of the reflection, F_{hkl} is the structure factor, W_{hkl} is the atomic displacement factor (ADP) (also known as the Debye-Waller factor or the temperature factor) and A_{hkl} is the absorption factor. The crucial term is the structure factor

$$F(hkl) = \sum_{n=1}^{N} f_n exp\left[2\pi i \left(hx_n + ky_n + lz_n\right)\right] \tag{2.2}$$

which may also be written

$$F(hkl) = \sum_{n=1}^{N} f_n \left(\cos 2\pi(hx_n + ky_n + lz_n) + i \sin 2\pi(hx_n + ky_n + lz_n)\right) \tag{2.3}$$

where f_n is the atomic scattering factor. The scattering factor varies depending on the type of radiation used, however there is also a reduction in peak intensity due to the thermal motion and/or disorder of atoms, which is parametrised in terms of the atomic displacement parameter. This motion or disorder causes a decrease in peak intensity with increasing angle, 2θ, since

$$f_B = f_a exp\left[-B\left(\frac{\sin\vartheta}{\lambda}\right)^2\right] \tag{2.4}$$

where $B = 8\pi^2\langle u^2\rangle$.

2.6.1 X-ray Diffraction

The diffraction of X-rays and neutrons are both described by Bragg's law, however there is one key difference; that X-rays interact with electrons, while neutrons interact with nuclei. The atomic X-ray scattering factor of an atom may be calculated from the electron density around the atom, and is directly proportional to its atomic number. The primary consequence of this is that isoelectronic ions or atoms have equal scattering powers, so F^- and Na^+ would be indistinguishable using X-ray diffraction. It also means that in structure solution, it is often difficult to accurately locate light atoms in the presence of heavier ones. The interaction of X-rays with electrons means that there is a decrease in intensity of the scattered beam with an increase in 2θ in a manner described by the atomic form factor:

$$f(\lambda,\theta) = Zg(Q)r_e \tag{2.5}$$

where Z is the atomic number, $g(Q)$ decays from 1 at the origin to 0 as $Q \to \infty$ and r_e is the classical radius of the electron.[61]

2.6.2 Neutron Diffraction

While the electromagnetic component of X-rays interacts with electrons, neutrons interact with the nuclei of atoms. One of the important results of this is that instead of the scattering factor f_n varying directly with Z as it does for X-ray scattering, the scattering factor for neutrons varies in a seemingly random manner. This means that

neutron diffraction is a very useful technique for locating certain atoms, in particular light atoms that are poor scatterers of X-rays such as hydrogen in the presence of heavier atoms. An atom may scatter neutrons either coherently or incoherently; coherent, elastic, scattering produces diffraction patterns in a similar manner to X-rays, incoherent scattering does not produce Bragg reflections and is a disadvantage for diffraction (though useful for other techniques, and particularly for the study of hydrogenous materials, as discussed in Section 2.9). A selection of relevant neutron scattering data for elements encountered in this Thesis is given in Table 2.2.[62]

Table 2.2: Selected neutron scattering data, given as coherent, incoherent, total and absorption cross sections. Absorption cross sections are quoted for neutrons with velocity 2200 ms^{-1} or energy of 25.3 meV.

Isotope	Abundance %	σ_{coh} barn	σ_{inc} barn	σ_{scatt} barn	σ_{abs} barn
^{1}H	99.985	1.7583	80.27	82.03	0.3326
^{2}H	0.015	5.592	2.05	7.64	0.000519
Li	-	0.454	0.92	1.37	70.5
^{6}Li	7.5	0.51	0.46	0.97	940
^{7}Li	92.5	0.619	0.78	1.4	0.0454
B	-	3.54	1.7	5.24	767
^{10}B	20	0.144	3	3.1	3835
^{11}B	80	5.56	0.21	5.77	0.0055
N	-	11.01	0.5	11.51	1.90
Mg	-	3.631	0.08	3.71	0.063
V	-	0.0203	5.07	5.09	4.9
Al	-	1.495	0.0082	1.503	0.231
Gd	-	29.3	151	180	49700

For experimentation, an important property of neutrons is their ability to penetrate a long distance through material, because they are charge neutral. This is with the caveat that, as shown in Table 2.2, some elemental isotopes absorb neutrons very strongly. High penetration is useful as it allows for the use of various demanding experimental sample environments. Cryostats, furnaces and other custom equipment such as the IGA^{n} described in Section 2.11.3 may be used and developed with simpler and more reliable engineering processes than for X-ray diffraction.

In structure completion (particularly in the location of deuterium atoms), neutron diffraction holds a final advantage. The small size of a nucleus compared to the wavelength of the neutron means that there is no angular dependence of the scattering factor as there is for X-ray scattering. Thus there is no drop-off in intensity of Bragg reflections with increased angle, resulting in more information available in neutron diffraction data compared with equivalent X-ray diffraction data.

2.6.3 Refinement of Structural Models

The process of structure solution from powder diffraction data used in this Thesis involved the following steps:

1. Obtain an accurate set of intensity values along with the position of all the Bragg reflections.

2. Determine the unit cell parameters, index the reflections, and determine the space group of the crystal.

3. Use chemical knowledge or intuition to create a possible structure model.

4. Compare the intensities or structure factors of the model with those obtained experimentally.

5. Adjust the atomic positions to obtain an improved agreement between the calculated and observed model, in an attempt to minimise the weighted profile R factor, R_{wp} as shown in Equation 2.8.

Within this general procedure, a more specific description of the methods used in this Thesis are detailed in the following sections.

Pawley Refinement

Pawley refinement is used to refine the unit cell from powder diffraction data.[63] Following indexing of a pattern, it is necessary to determine the precise unit cell parameters and compare the possible space groups. A Pawley refinement varies the peak profile and unit cell parameters to obtain the best possible fit to observed data, the output is a list of (hkl) values, their positions and intensities. The intensity of the (hkl) peaks can be used effectively to compare different space groups, and to monitor the changes in a phase where the atomic positions are unknown. It is particularly useful where peak overlap would make this process challenging to achieve by inspection alone.

Simulated Annealing

Simulated annealing is a very useful procedure that may be used to gain an initial structure when an obvious starting point for atomic positions in a Rietveld refinement is non-trivial. It is a global optimisation technique, that searches for the optimal solution among many possible solutions in a large search space. While in normal refinement methods, the solution can only travel "downhill," in simulated annealing "uphill" steps are also allowed, which means that the refinement can escape from local minima. Uphill steps are introduced by replacing a current solution with a random nearby one. By analogy with physical annealing, a hypothetical temperature is used to control the movement of the trial solutions. In the case of structure solution, this "temperature" is in the units of the minimising function, R_{wp}. Higher "temperatures" allow atoms to move far from their original positions and extensively explore the parameter space. An annealing regime is used to lower the "temperature" slowly so that downhill moves are increasingly preferred as low R_{wp} solutions are increasingly explored. During this process, it is often convenient to describe the relative coordinates of known chemical units as rigid bodies, say

NH_3 or BH_4^-, and allow these to move around the unit cell, allowing a great deal of possible solutions to be explored relatively quickly.

Rietveld Refinement

Rietveld refinement is used for the refinement of the final atomic positions, thermal parameters, and other desired values within a now fixed unit cell. The basic principle of the method is to minimise the function M (Equation 2.6), that is the difference between the calculated profile and the observed data

$$M = \sum_i W_i \left\{ y_i^{obs} - \frac{1}{c} y_i^{calc} \right\}^2 \tag{2.6}$$

where y^{obs} and y^{calc} are observed and calculated data and W is a weighting parameter.[64] The quality of the fit of the model to the data is typically expressed using one or all of a few key statistical parameters.[65] The perfect fit is obtained when the expected R-value (R_{exp}) is equal to the weighted profile R-value (R_{wp}).

$$R_p = \sqrt{\frac{\sum |Y_{o,m} - Y_{c,m}|}{\sum Y_{o,m}^2}} \tag{2.7}$$

$$R_{wp} = \sqrt{\frac{\sum w_m (Y_{o,m} - Y_{c,m})^2}{\sum w_m Y_{o,m}^2}} \tag{2.8}$$

$$R_{exp} = \sqrt{\frac{M - P}{w_m Y_(o,m)^2}} \tag{2.9}$$

$$GOF = \chi^2 = \frac{R_{wp}}{R_{exp}} \sqrt{\frac{\sum w_m (Y_{o,m} - Y_{c,m})^2}{\sum M - P}} \tag{2.10}$$

where $Y_{o,m}$ and $Y_{c,m}$ are observed and calculated data respectively at point m, w_m is the weighting given to point m (which is given by $w_m = 1/\sigma(Y_{(o,m)})^2$), M is

the number of data and P is the number of parameters. Of these parameters, χ^2 is perhaps the most useful as it accounts for the quality of the fit against the number of refineable parameters. Thus avoiding the pitfall of obtaining a good fit to diffraction data by simply including a vast number of irrelevant refineable parameters. While a certain amount of experience is required to say if a model is correct, and a good visual fit to he data is important, a value of $\chi^2 < 3$ is an indicator of a good fit. While an accompanying R_{wp} value of < 10 is indicative of a well-fitted profile with a relatively low background. These statistics are particularly useful in determining the presence of subtle structural features.

2.6.4 Computational Methods

A variety of programs were used to implement the methods discussed above, the programs used were Topas Academic,[66] DASH,[67] and Crystals.[68]

Topas Academic

Topas was used for analysis of all powder diffraction data including; indexing of patterns, Pawley refinement and Rietveld refinement. Topas has a number of advantages as a diffraction analysis program, it adopts a language that is both powerful and flexible enabling the easy introduction of non-standard models. The ability to perform batch refinements, using the output of a first refinement as the input to the second and so on, is also useful in analysing large numbers of diffraction patterns in a consistent manner.

DASH

Dash was used for structural solution from X-ray diffraction data, it employs a Bayesian ranking procedure in indexing and space group analyis. With the use of rigid bodies, the inbuilt simulated annealing process often yields good results for

further Rietveld refinement.

Crystals

Crystals was used for analysis of single crystal diffraction data with the assistance of Dr. Francesco Fabbiani. In particular the Annulus model built into the program was used to model delocalised rings of electron density rather than "discrete" atoms within molecules.[69]

2.6.5 Instrumentation: X-ray Facilities

All X-ray powder diffraction data were collected using synchrotron radiation sources, while the single crystal data were collected using standard laboratory equipment. In a synchrotron, electrons fired from an electron gun are accelerated by a linear accelerator and then a booster synchrotron ring until they approach the speed of light, when they are released into a storage ring. The storage ring consists of straight sections and bending magnets. When the electron path is bent, Brehmstahlung radiation is emitted.[70,71] The type of Brehmstahlung radiation emitted depends on the strength of the magnetic field and the speed of the electrons, in this case X-rays are produced. The wavelength of the X-rays is further tuned by passing through a Si (111) monochromator crystal.[72,73] This tuning process is repeated in each beam cycle, so different experiments are likely to have been carried out using different wavelength X-rays.

In the laboratory based diffractometer, X-rays are produced by firing a beam of electrons, produced by an electron gun, at a metal source. The source is typically a transition metal, and X-rays are produced by absorption and excitation of electrons followed by relaxation of electrons and emission of radiation. Thus the wavelength produced depends on the metal chosen and the energy levels of its orbitals.

The advantage of using a synchrotron X-ray source is that the high intensity

allows short data collection times and a vastly improved signal to noise ratio, this is useful for studying both materials which are poor scatters of X-rays and kinetics of phase changes. There are some problems with using such powerful X-rays; the beam is prone to heat samples meaning that temperature readings may be prone to slight error, in some cases severe beam damage can also occur and result in structural changes or the destruction of samples as shown in Figure 2.3.[74]

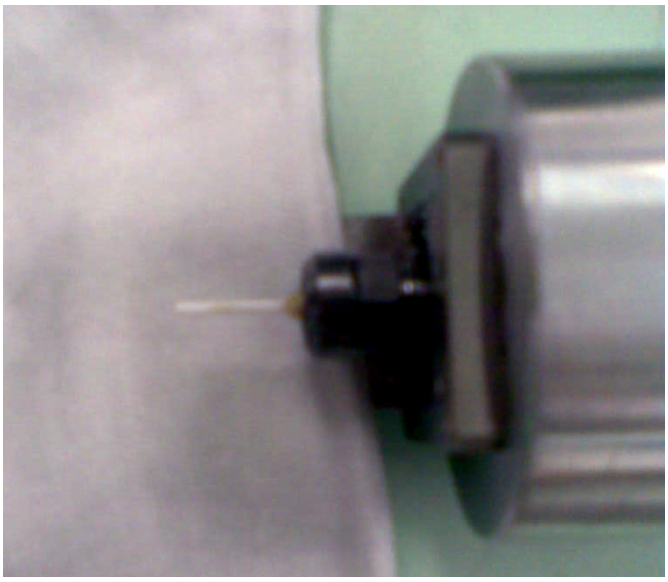

Figure 2.3: A picture showing a sample of $Mg(NH_3)_6Cl_2$ in a capillary tube after data collection at the ESRF beamline ID31, the discolouration of the sample near the centre of the capillary indicates beam damage has occurred.

European Synchrotron Radiation Facility[72]

European Synchrotron Radiation Facility (ESRF) data were collected on the ID31 beamline, which operates at an energy range of between 5 and 60 keV. Diffraction data were collected using a wavelength of around 0.8 Å and a step-size of 0.003 °. A bank of nine scintillation detectors, each spaced ca. 2 ° apart, measure the diffracted intensity as a function of 2θ, with each detector preceded by a Ge (111) crystal analyser. The nine crystals are mounted on a single rotation stage so that only a single adjustment is to obtain a maximum range of diffraction data.

The diffractometer was operated in Debye-Scherrer transmission geometry. Samples were loaded into borosilicate glass capillary tubes (diameter 0.8 mm - 1.0 mm) within a nitrogen atmosphere glove bag. The capillaries were then packed with a glass rod to prevent sample movement and temporarily sealed using vacuum grease. After removal from the glove bag, the capillaries were sealed permanently using a natural gas-oxygen flame. The capillaries were rotated in the beam during data collection in order to provide a good powder average of intensities. Diffraction data were collected either at room temperature or during in-situ variable temperature experiments. Samples were heated by an Oxford Cryostreams cold-nitrogen-gas-blower (-193 °C to 227 °C, or 80 K to 500 K) or a Cyberstar hot-air blower (up to 950 °C).

Diamond Light Source[73]

Diamond light source data were collected on beamline I-11. The beamline is shown in Figure 2.4 and is very similar to ID31 at the ESRF, as described above. Electrons are accelerated to approximately 30 eV under ultra high vacuum (10^{-13} bar), the resultant X-rays have energies of between 5 and 30 keV. A wavelength of around 0.8 Å was selected and a bank of nine detectors was used. The samples were prepared in the same manner as those for the ESRF, except that 0.7 mm capillary tubes were used and no glass rod was used to pack the samples.

Single crystal X-ray diffraction

Single crystal data were collected at 150 K on a Nonius Kappa CCD diffractometer (λ = 0.71073 Å) equipped with a Oxford Cryosystems low-temperature device. Suitable crystals were selected by eye and mounted on the sample holder using hair and paraffin wax, with the assistance of Dr. Amber Thompson. Crystals were mounted on a laboratory bench where a stream of argon gas was blown over the

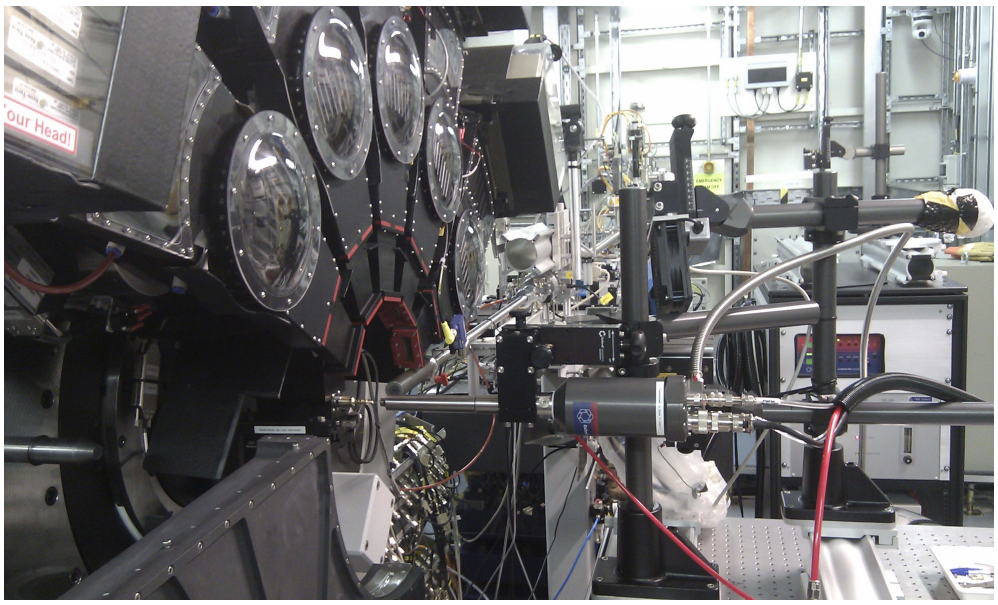

Figure 2.4: The experimental set-up of I11 at Diamond Light Source

sample in an attempt to maintain an inert atmosphere. During data collection, the inert atmosphere was maintained via the nitrogen gas cryostream.

2.7 ISIS Spallation Neutron Source[75]

It is possible to produce neutrons in a reactor by fission reactions, or to use a spallation source. Neutron experiments in this Thesis were carried out at the ISIS spallation neutron source. First H^- ions are produced by an electric discharge, and initially accelerated using a Radio Frequency Quadrupole accelerator which also divides the ions into bunches. Bunches of ions are further accelerated to 37 % of the speed of light in a linear accelerator. The accelerated ions enter a synchrotron through an alumina foil which removes the electrons, leaving protons. In the synchrotron the protons are accelerated to 86 % of the speed of light by ten radio frequency electric field cavities. When the protons reach the required speed they are extracted by kicker magnets towards the targets. The extracted protons hit the tungsten metal target causing neutrons to be ejected. Moderators are used to slow

down the neutrons to the appropriate energy levels for the required experiments. The neutrons from Target Station One pass through one of four moderators. Two of these moderators use room temperature water, one contains methane at 100 K and the other contains liquid hydrogen at 20 K. The moderators are about 0.5 L in volume and are surrounded by water-cooled beryllium reflectors which scatter divergent neutrons back into the moderator, this increases the flux of neutrons leaving the moderator and moving towards the individual beam lines and experiments.

At reactor neutron sources the neutrons produced are monochromated for use in experiments, whilst at ISIS 'white' neutrons with a range of wavelengths are used. As the source produces pulses of neutrons, data are collected as a function of time-of-flight. Combining Bragg's Law with the de Broglie relationship (Equation 2.11) and substituting values for Planck's constant and the neutron mass Equation 2.12 is obtained

$$\lambda = \frac{h}{mv} \tag{2.11}$$

$$t = 505.56Ld\sin\theta \tag{2.12}$$

where time-of-flight (t) is measured in microseconds, flight path (L) in metres and d-spacing (d) in Ångstrom units.[76] Fixed detector banks are used, each with its own characteristic resolution and d-spacing range. An advantage of having fixed detectors is that it is possible to use a sample environment that blocks off certain angles, as long as others remain clear. The neutron pulse provides a large number of high energy neutrons, which means that very small d-spacings are accessible on diffractometers. The resolution function for a time-of-flight diffractometer is well-approximated by the formula,

$$\frac{\Delta d}{d} = \left(\left(\frac{\Delta t}{t} \right)^2 + \left(\frac{\Delta L}{L} \right)^2 + (\Delta\theta \cot\theta)^2 \right)^{(1/2)} \tag{2.13}$$

where Δd is the width of a reflection at a d-spacing, d. The first term is approximately constant for a given moderator.[76] The second term arises from uncertainties in the flight path, and is constant for a given measurement, increasing the flight path will increase resolution but at the expense of neutron flux. The angular dispersion term arises because finite widths of the sample and detector mean that a range of wavelengths satisfy the Bragg condition for each reflection. At low angles (large $\cot\theta$) this term dominates, but it becomes vanishingly small at high angles.

2.7.1 General Materials Diffractometer[77]

The General Materials Diffractometer, or GEM, was designed to be a high intensity, high resolution neutron diffractometer for both disordered materials and crystalline powders. The flight path from moderator to sample is 17 m which provides a high resolution. The 8 detector banks positioned at angles between 1.1 ° and 169.3 ° are further described in Table 2.3 and shown in Figure 2.5. The range of d-spacings accessible are 0.1 Å to ca. 15 Å. One of its advantages is the large (12 m^2) detector area which means that high quality diffraction data are obtained in a matter of minutes, making this the ideal instrument for kinetic and disordered material studies.

2.7.2 High Resolution Powder Diffractometer[76]

The High Resolution Powder Diffractometer, or HRPD, at ISIS is the finest diffractometer of its kind in the world, and the quality of the data is such that structure solution is possible for samples that would normally require corroboratory single crystal or X-ray diffraction data. It is positioned at the end of a 100 m long ^{58}Ni super mirror neutron guide, and this exceptionally long flight path gives rise to a

Table 2.3: The detector specifications for the GEM diffractometer.

Bank	Mean Angle 2θ	Min Angle °	Max Angle °	L_2 m	Resolution $\Delta Q/Q$ %
0	-	1.1	3.2	2.8-2.9	5-10
1	9	5.6	12.5	2.2-2.4	4.7
2	17	13.8	21.0	1.48-2.10	2.4
3	34	24.8	45.0	0.65-1.40	1.7-2
4	62	49.9	74.9	1.03-1.44	0.79
5	92	79.0	104.0	1.38	0.51
5X	109	105.5	113.5	1.38	0.51
6	146	141.9	149.2	1.54-1.74	0.34
7	159	149.3	169.3	1.04-1.39	0.35

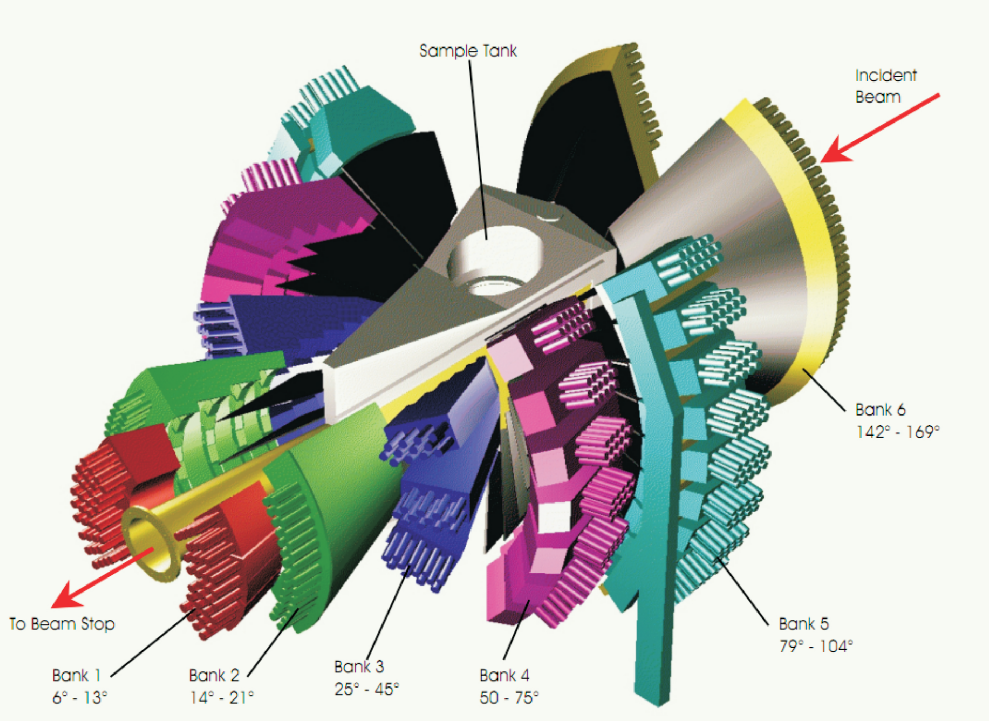

Figure 2.5: A diagram showing the orientation of the GEM diffractometer detector banks.[75]

very high resolution of $\Delta d/d \approx 4 \times 10^{-4}$. The long flight path means that subsequent neutron pulses are able overlap, to eliminate this undesirable overlap beam choppers are in place on the neutron guide, two chopper settings are available to select the desired range of neutron energies. An overall d-spacing range of 0.6-16.5 Å is accessible, though the highest resolution data of the back scattering bank is only available up to approximately 4.6 Å. There are three detector banks, positioned at 30 ° (bank 3), 90 ° (bank 2), and 168 ° (bank 1), that provide a range of resolutions and d-spacing ranges; the 90 ° bank offers the best count statistics while the 168 ° bank provides the highest resolution data (this is illustrated in Section 2.11.3, Figure 2.11). The instrumental configuration is shown in Figure 2.6.

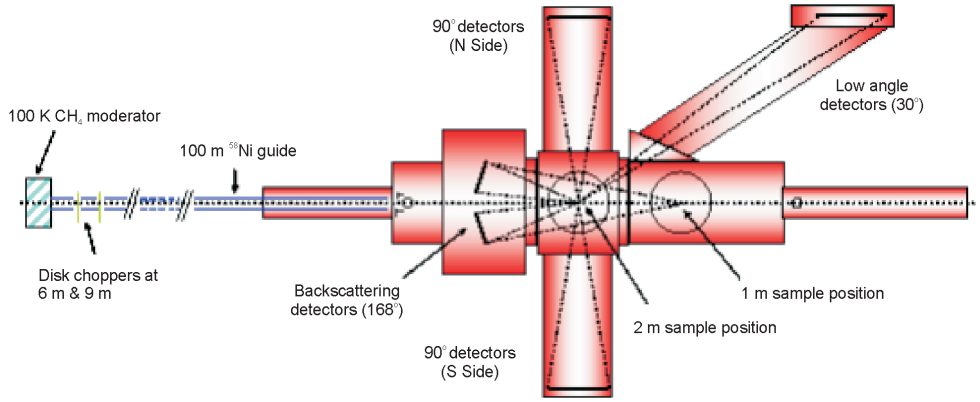

Figure 2.6: A schematic diagram of HRPD.[76]

Low temperature studies of $Mg(ND_3)_6Cl_2$ and $Mg(ND_3)_6(^{11}BD_4)_2$ were carried out using the in-house closed cycle refrigerators and cryostats to control the sample temperature between 4 K and 300 K.

2.8 Raman Spectroscopy[78,79]

During Raman spectroscopy a sample is exposed to intense single wavelength radiation. On impact with a molecule, photons with less energy than that required to promote an electron into an excited state may cause excitation of that electron

into a virtual excited state. This virtual state has a short lifetime, and the majority of absorbed light is re-emitted at the same energy (it is scattered elastically with v_0). However a small proportion of emitted light differs from the incident by an energy equivalent to some of the vibrational modes of the molecule (it is scattered inelastically with $v_0 \pm hv$). This is the Raman effect, and its concept is shown in Figure 2.7. The effect is very weak, meaning that a very intense monochromted light is required, so a laser source is usually used in spectroscopy.

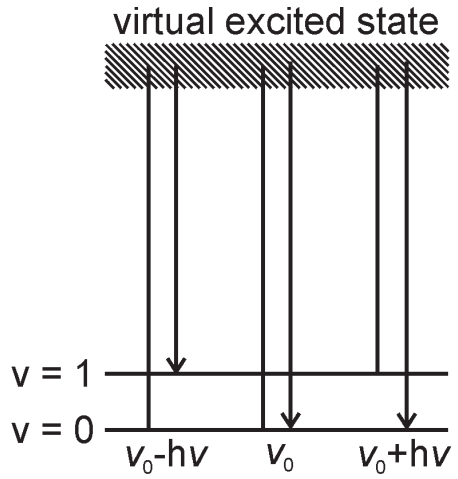

Figure 2.7: A diagram showing the concept of Raman scattering.

With respect to this Thesis, the useful result of this effect is that the scattered photons differ in wavelength from the incident beam by a vibrational frequency of the molecule in question. Assuming that the vibrations are accurately described by a quantum harmonic oscillator experiencing a force $F = kx^2$, then the energies of these modes are described by Equations 2.14 and 2.15. It should also be noted that only vibrational modes that correspond to a change in the polarisability of the molecule are active in Raman spectroscopy. Raman spectra in this Thesis were recorded with a Dilor Labram 300 spectrometer, equipped with a CCD detector, and using a wavelength of $\lambda = 514.5$ nm. Samples were loaded into glass capillaries in an inert argon atmosphere and sealed using a gas-oxygen flame before data collection.

$$E = \hbar\omega(v + 1/2) \tag{2.14}$$

$$\omega = \frac{1}{2\pi}\sqrt{\frac{k}{\mu}} \tag{2.15}$$

where

$$\mu = \frac{m_1 \times m_2}{m_1 + m_2}$$

2.9 Inelastic Neutron Scattering[80–82]

While diffraction techniques utilise elastic scattering of neutrons, the energy gained or lost in inelastic scattering can be used in vibrational spectroscopy. A beam of neutrons with an appropriate and known velocity will pass through and transfer energy to or from a sample. The energy transfer which occurs can be written,

$$E = \hbar\omega = \tilde{v}hc = \frac{m_n |v|^2}{2} \tag{2.16}$$

$$E = \frac{\hbar |k|^2}{2m_n} \tag{2.17}$$

The incident neutron, of energy E_i, strikes the sample and after interaction has an energy E_f. The experiments in this Thesis were all carried out at low temperatures (ca. 20 K), so the incident neutron loses energy to the sample. Where the excitation of the sample is due to vibrational motions, the method is very similar to infra-red absorption spectroscopy, or Raman scattering.

While INS is conceptually similar to Raman scattering, there are significant differences in detail. The major difference, as discussed in Section 2.6, is that photons (electromagnetic radiation) interact primarily with the electrons, while neutrons interact with nuclei, so the strength of the interaction is dependent on the particular

nuclide involved. Another difference is that the wavelength of the electromagnetic radiation used for Raman experiments is in the visible or near UV region and is of the order of hundreds of nanometers (thousands of Ångstroms). The neutrons used in these experiments have wavelengths of 0.1 Å to 2 Å. This means that the size of the neutron is comparable to, or less than, the spacing between atoms and results in there being no "selection rules" as there are for optical spectroscopy.

Despite the complexities of neutron scattering, the INS technique can be simply summarised. The observed positions of transitions (the eigenvalues) are a function of the molecular structure and intramolecular forces, and correspond to energies lost from the neutron. The strength of a transition is a function of the atomic displacement occurring during the vibration (the eigenvector) and the momentum lost by the neutron. The atomic displacements are determined by the molecular structure and intramolecular forces, and the momentum transferred is determined by the neutron spectrometer. As a consequence, INS gives direct access to both the vibrational eigenvectors and eigenvalues.[80]

The geometry of an INS spectrometer allows for a beam of neutrons to fall on a sample and be scattered onto a detector, of area A, at distance, d_f, and an angle, θ, relative to the sample and the incident beam. These values (d_f, θ) are the polar coordinates for the system, for which the solid angle $d\Omega$ (subtended by an angular element, $d\theta$) is $2\pi \sin\theta d\theta$.[80] The spectrometer scans the energy spectrum of the sample and records the flux in neutrons measured per second, this is the final neutron flux, J_f, and is normalised relative to the incident flux, J_i. The sample's response is a function of energy, E, and since the polar coordinates of the detector can be changed, is also a function of solid angle.[80] The observable is the rate of change of the cross section with respect to the final energy, E_f, and solid angle, $d\Omega$, known as the double differential scattering cross section:

$$\frac{d^2\sigma}{dE_f d\Omega}$$

where

$$d\Omega = \frac{A}{d_f^2}$$

This double differential is employed in the Scattering Law which relates the momentum transfer vector, Q, and the wavenumber, ω, to the observable intensities:

$$S(\mathbf{Q},\omega)_l = \frac{4\pi}{\sigma_l}\frac{\mathbf{k_i}}{\mathbf{k_f}}\left(\frac{d^2\Omega}{dE_f d\Omega}\right)_l \tag{2.18}$$

where σ_l is the scattering cross section of atom l and $\mathbf{k_i}$ and $\mathbf{k_f}$ are the momenta of the incident and final neutrons respectively.

Typically, spectroscopic intensities are reported as $S(\mathbf{Q},\omega)$, which is related to the amplitude of the cross section weighted density of states. For a single molecule containing N atoms,

$$S(\mathbf{Q},\omega)_{total} = y\sum_{l=1}^{N} S(\mathbf{Q},\omega)_l\sigma_l = 4\pi\frac{\mathbf{k_i}}{\mathbf{k_f}}\left(\frac{d^2\sigma}{dE_f d\Omega}\right)_{observed} \tag{2.19}$$

The intensities, $S(\mathbf{Q},\omega)$, are reported in scaled units, that are related to the actual units, barn $(\mathrm{cm}^{-1})^{-1}$, by the linear factor y. The spectra become unitless and are therefore compared in terms of relative intensities. When powder samples are used then the powder averaged scattering law is

$$S(\mathbf{Q},\omega)_{powder} = \frac{1}{4\pi}\int S(\mathbf{Q},\omega)d\mathbf{Q} \tag{2.20}$$

Inelastic neutron spectroscopy has several advantages over analogous optical techniques:

1. INS spectra can be accurately modelled using molecular dynamics software and the intensities measured during an experiment can be straightforwardly related to the atomic displacements of the scattering atoms. This is because complications arising from electro-optic parameters are avoided. This also means that the spectra are quantitative, so for example one spectra may be subtracted from another to reveal the spectra of a second phase.

2. The technique is sensitive to hydrogen atoms (^{1}H) due to their large incoherent scattering cross section (see Section 2.6.2). Optical techniques tend to be more sensitive to larger, more electron-rich atoms.

3. There are no optical selection rules for INS, so in principle, all molecular vibrations are observable.

4. The high penetration of neutrons means that they pass readily through sample holders and into the bulk of samples, thus information on the bulk properties of samples is obtained.

5. There is a very wide spectral range available (16 cm^{-1} to 4000 cm^{-1}), that covers the entire molecular range. The reliability of measurements at low wavenumbers is greatly increased over optical techniques.

2.9.1 TOSCA[82]

INS measurements discussed in this work were collected using the TOSCA Spectrometer at the ISIS pulsed neutron facility. TOSCA is an indirect geometry spectrometer optimised for the study of molecular vibrations in the solid state, it has an energy range of 0 cm^{-1} to 4000 cm^{-1} (0 meV to 500 meV), but gives best results below 2000 cm^{-1} (250 meV). Samples were crash-cooled using liquid helium before data were collected at ca. 20 K; this low temperature was chosen to reduce the thermal effects that degrade the spectra.

2.10 Nuclear Magnetic Resonance[78,83,84]

Nuclear magnetic resonance (NMR) spectroscopy measures the interaction of the nuclear spin of an atomic nucleus with an applied magnetic field and the nuclear spin of surrounding nuclei. In a magnetic field, there are 2I + 1 spin states that are non-degenerate (where I is the nuclear spin quantum number). Radio frequency irradiation at the NMR frequency causes transitions between these states, as shown in Equation 2.21 and Figure 2.8;

$$\Delta E = \hbar\gamma B = hv \tag{2.21}$$

$$v_{NMR} = \frac{\gamma B}{2\pi}$$

where B is the applied magnetic field and γ is the gyromagnetic ratio of the nuclide in question. As a technique, sensitivity is considered low due to the small population difference between the spin states. The receptivity of a nuclide is determined by both the gyromagnetic ratio and the abundance of the nuclide, data for nuclei relevant to this Thesis are given at the end of this Section in Table 2.4.

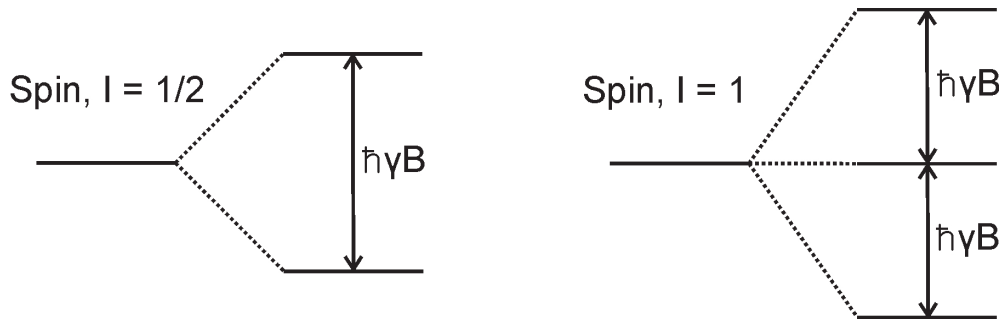

Figure 2.8: A diagram showing the splitting of energy levels in a nuclide in a magnetic field, with spin I = 1/2 and spin I = 1 on the left and right respectively.

The peaks in NMR spectra are reported using a chemical shift, as defined in Equation 2.22. It is clear from Equation 2.21 that the chemical shift depends on the nuclei, and introducing a shielding constant σ as shown in Equation 2.23 accounts for

the fact that the local environment of a nucleus also effects the chemical shift. Many factors affect shielding, but in this Thesis the important factor is that electrons have a charge and will move in response to a magnetic field to generate an opposing field. This means that electrons shield nuclei from the magnetic field so in electron-rich environments σ is large and transitions occur at a lower radio frequency and a lower (more negative) chemical shift. Conversely if electron density is decreased, shielding is lower and chemical shift is higher (more positive).

$$\delta_{ppm} = \frac{\upsilon_{signal} - \upsilon_{reference}}{\upsilon_{spectrometer}} \times 10^6 \tag{2.22}$$

$$\upsilon = \frac{\gamma B(1-\sigma)}{2\pi} \tag{2.23}$$

Another important feature of an NMR spectrum is spin-spin or J- coupling. This occurs when an NMR active nucleus (A) is bonded to another active nucleus (X), the nucleus in question (A) will experience a range of magnetic fields, with the spectral result that signals will be split into 2I + 1 peaks (where I refers to the spin of the second nucleus (X)). The strength of the coupling varies depending on many factors but is strongest when two nuclei are covalently bonded together, it is reported as the coupling constant, J, with the units Hz. This coupling is demonstrated in Figure 2.9, where the coupling of A to a single nucleus X with I = 1 is shown to produce three peaks of even intensity, while coupling of A to 2 equivalent nuclei X with I = 1/2 produces a 1:2:1 triplet.

A further type of interaction is dipolar coupling, that originates from the through space interaction of magnetic nuclei and carries an angular dependence. In liquids this is effectively averaged to zero by molecular tumbling but in solids molecular motions are restricted, what should be equivalent nuclei actually have slightly different electronic environments thence dipolar interactions may result in a broad

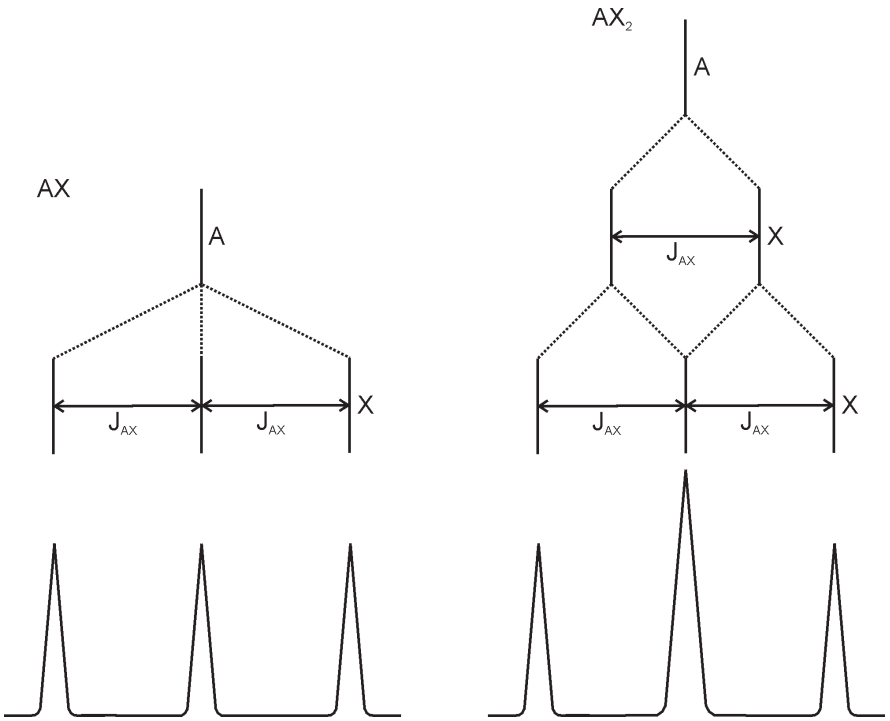

Figure 2.9: A diagram showing spin-sin coupling in the spectra of A in AX and AX_2, where $I_X = 1$ and $1/2$ respectively.

featureless spectra. It is possible to sharpen the features of such a broad spectra by imposing motion on the nuclei and rapidly spinning the sample, and this achieves best results when the spinning axis is at an angle of 54.7 ° to the applied magnetic field.[85] The reason for the sharpest spectra appearing at this so called "magic angle" is that when nuclei are in a strong magnetic field all nuclear spins align with the field. Any pair of nuclear spins are then effectively separated by a distance r and an angle θ to the magnetic field and the strength of dipolar coupling is given by relationship shown in Equation 2.24. Dipolar coupling may be effectively removed when the sample is spun at $\beta = 54.7°$ as $3\cos^2\beta - 1 = 0$. This spinning technique for solid-state NMR spectroscopy is widely known as magic angle spinning (MAS).

$$d \propto \frac{3\cos^2\beta - 1}{2r^3} \tag{2.24}$$

A final effect to consider is that caused by quadrupolar nuclei; any nuclei with

a spin greater than 1/2 possess a non-spherical charge distribution or quadrupole. The important difference between dipolar and quadrupolar nuclei is that a dipole interacts with electric fields but a quadrupole interacts with field gradients. In solids the electric field gradient at a nucleus depends on the site symmetry and the non-uniform distribution of charge. For example a nucleus in a high symmetry octahedral site will not feel any net quadrupolar interaction, but two negative charges close to the nucleus can produce a quadrupolar interaction that causes line splitting in the spectra of single-crystals and line broadening in the spectra of powder or disordered samples. This is in fact a 2^{nd} order effect, 1^{st} order effects cause additional splitting in the nuclear energy levels with the spectral result that satellite transitions known as as spinning side-bands are observed, though it is possible for these to be averaged by MAS in a similar manner to dipolar coupling. In liquids, molecular tumbling causes quadrupolar nuclei to relax very quickly resulting in no spin-spin coupling being observed and instead the appearance of broad spectral lines.

Table 2.4: NMR data for nuclei relevant to this Thesis

Isotope	Abundance %	Spin Quantum Number I	Gyromagnetic Ratio γ $10^7 T^{-1}s^{-1}$	Receptivity relative to ^{1}H
^{1}H	99.985	1/2	36.752	1.00
^{10}B	20	3	2.874	3.95×10^{-3}
^{11}B	80	3/2	8.584	1.32×10^{-1}
^{14}N	99.6	1	1.934	1.01×10^{-3}
^{15}N	0.37	1/2	-2.713	3.85×10^{-6}
^{25}Mg	10	5/2	-1.634	2.68×10^{-4}

2.10.1 Solid State NMR

Solid state ^{25}Mg NMR measurements of MgX_2 and $Mg(NH_3)_6X_2$ were carried out by the EPSRC Solid-state NMR Service at Durham University. Measurements were performed at 24.48 MHz, using a pulse-acquire sequence with a 4 μs (30 °) pulse and referenced to a 1 M solution of $MgCl_2(H_2O)_{6\,(aq)}$.

2.10.2 Solution State NMR

Solution state ^{1}H NMR measurements of $Li(NH_3)BH_4$ were carried out using a Varian Mercury 300 MHz spectrometer. Samples were loaded into NMR tubes within a nitrogen atmosphere glove-bag, dissolved in dry THF-d_8, sealed temporarily with a Young's tap and then sealed permanently with a natural-gas-oxygen flame.

2.11 Gravimetric Analysis Techniques

Gravimetric analysis techniques were used to investigate both the decomposition temperatures and pathways of compounds. Two techniques were used, thermogravimetric analysis (TGA) and intelligent gravimetric analysis (IGA). Both techniques record sample mass as a function of time or temperature, while with IGA it is also possible to control the pressure of a static or flowing gas in the sample chamber. One of the weaknesses of these techniques in general is the ill defined process determining the decomposition temperature. In this Thesis, the definitions onset temperature (T_o) and peak temperature (T_p) are used throughout. Onset temperature is calculated from a plot of m *vs.* T and is defined as the intersection between the straight tangential lines drawn from the plateau mass and from the point of peak mass loss, as shown in Figure 2.10. Peak temperature is defined as the minimum on the section of the first derivative curve ($\frac{dm}{dT}$) relevant to the corresponding mass loss and is also shown in Figure 2.10.

2.11.1 Thermogravimetric Analysis

Thermogravimetric analysis (TGA) was carried out using a Setaram SETSYS Evolution Thermogravimetric Analyser. The analyser was housed in a custom built nitrogen atmosphere glovebox with an oxygen content kept below 10 ppm by maintaining a constant flow of nitrogen gas. Powder samples of approximately 20 mg were first

loaded into a platinum crucible in an argon atmosphere glovebox, and transferred to the analyser glove box in a sample jar sealed with Parafilm®. Measurements were carried out under an argon atmosphere flowing at a rate of 10 $\mathrm{mlmin^{-1}}$ and with a typical heating rate of 2 $\mathrm{^{\circ}Cmin^{-1}}$.

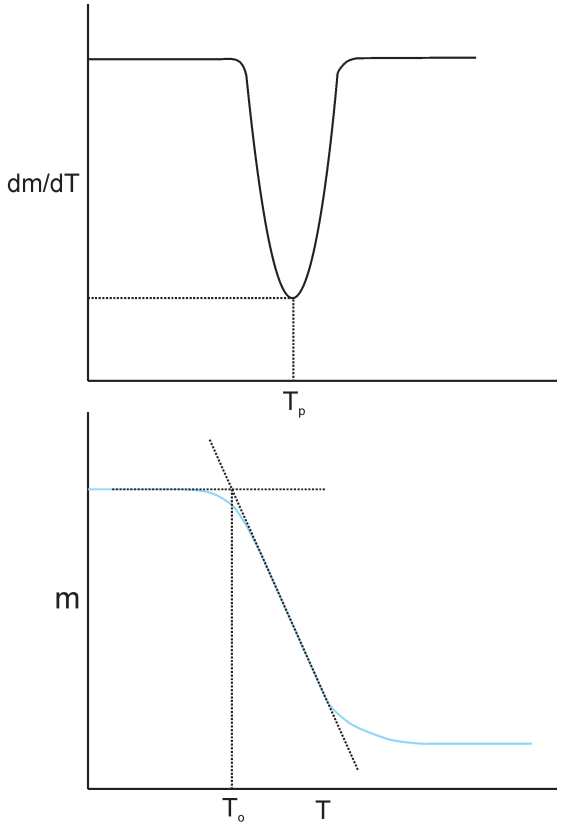

Figure 2.10: A diagram showing the definitions of T_p and T_o that are used to describe the results of gravimetric analysis experiments in this Thesis.

2.11.2 Residual Gas Analysis

Residual gas analysis (RGA) of $Mg(NH_3)_6(BH_4)_2$ was used to compliment TGA data. Measurements were carried out at Birmingham University using a "home built" temperature programmed desorption apparatus coupled to a quadrupole mass spectrometer (Thermo Electron, VG ProLab). Inside an argon atmosphere glovebox, samples of approximately 0.2 g were loaded into a quartz reaction tube that was sealed at one end. This was positioned vertically in the reaction chamber, removed

from the glovebox and loaded onto the apparatus without exposing the sample to air. Measurements took place under an argon atmosphere with a flow rate of 100 $mlmin^{-1}$. The sample was heated at 2 $°Cmin^{-1}$ up to 370 °C and held at this temperature until gas desorption had stopped. A heated capillary was used to sample the desorbed gas species in the argon flow on the downstream side of the reaction vessel. The Faraday detector of the mass spectrometer was used to record mass channels of 2 (H_2^+), 16 (NH_2^+) 17 (NH_3^+ or OH^+), 18 (H_2O^+), 28 (N_2^+), 32 (O_2^+) and 40 (Ar^+).[86]

2.11.3 In-Situ Gravimetric Analysis and Neutron Diffraction

A collaboration between the ISIS Facility, University of Oxford and Hiden Analytical has resulted in the design and commissioning of an intelligent gravimetric analyser (IGA) which can be used on GEM and HRPD the neutron diffractometers at ISIS (the IGA^n). The instrument allows simultaneous collection of thermogravimetric and neutron diffraction data, as a function of pressure, temperature, or time. The combination of these data allows for a more detailed analysis of both diffraction and thermogravimetric data than would be possible using either technique alone. The variety of temperature and pressure regimes accessible using a single instrument allows for greater experimental flexibility and more thorough phase characterisation.

The sample container for the IGA^n is a thin quartz or vanadium bucket, the quartz bucket was used as a standard during the commissioning of vanadium buckets. The reaction vessel is fitted with a standard Tomkinson flange, which allows it to be fitted into the GEM and HRPD beamlines, as well as a custom built argon atmosphere glovebox which allows for loading and unloading of air sensitive samples. The temperature is varied using two band heating elements which are located inside the reaction vessel above and below the sample. The heaters are positioned to ensure minimum interaction with the neutron beam.

Weighed amounts (0.1 - 1.0 g) of a thoroughly ground sample were loaded into the sample holder in an argon atmosphere glovebox, and then transferred to the IGA^{n} glovebox using an airtight container. The IGA^{n} glovebox was purged with argon gas for 30 minutes before the sample holder was loaded on to the tungsten hang down wire, and the reactor vessel was sealed via the Tomkinson flange. The set-up was then craned out of the glovebox and into the diffraction chamber.

For experiments involving $Li(ND_3)^{11}_{n}BD_4$ on GEM, neutron diffraction data were collected continuously over periods of 3 minutes. For experiments involving $Li(ND_3)^{11}_{n}BD_4$ on HRPD, neutron diffraction data were collected continuously over periods of 10 minutes. At various pressures and temperatures, isothermic and isobaric diffraction data were collected for extended periods of time in order to improve the signal to noise ratio within these data. Thermogravimetric data were recorded approximately every 10 seconds, with the measured mass accurate to ± 0.0001 mg and the measured temperature and pressure accurate to ± 0.001°C and ± 0.01 mbar respectively. During some experiments the IGA^{n} was used without neutron diffraction, operation in this mode is denoted by the acronym IGA. Two distinct pressure regimes were used during experiments, these were: application of a static pressure of gas, and application of a dynamic vacuum where the sample vessel was continuously exposed to a vacuum pump, an operation known as 'outgas.'

Despite its potential as a very powerful technique, the IGA^{n} system has a number of limitations; the primary ones are *i*) the instrument is not linked to the diffractometer (as in house built furnaces, cryostats etc. often are), so when using a spallation neutron source (as opposed to a reactor source) which is prone to occasional 'beam off' period, there is a significant risk that crucial collection of data occurring around a phase transition or decomposition may be missed. Though this is as much a limitation of using a spallation source for kinetic measurements as it is an issue with the instrumentation; and *ii*) the use of the steel reactor, which despite being designed to be wide enough that the collimators in GEM would effectively remove any Bragg

reflections caused by the steel, still meant that intense steel reflections were present in the diffraction data.

The problem of using the steel reactor was solved by the commissioning of a quartz reactor tube that was used in the HRPD experiments. However, the steel elements of the furnace still produced Bragg reflections in the diffraction data as shown in Figure 2.11. The application of gadolinium to the reactor vessel, as shown in Figure 2.12, enabled partial shielding of the steel elements, though given limited instrument commissioning time, it was not possible to consistently avoid the appearance of steel reflections in the diffraction data.

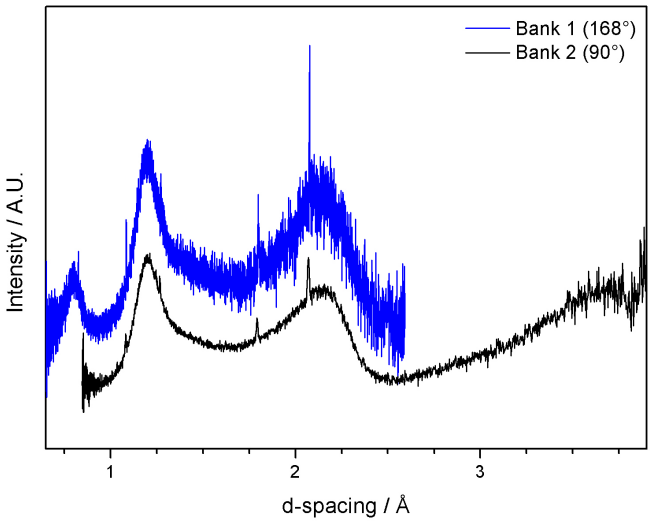

Figure 2.11: Diffraction data for the empty IGA^{n} apparatus fitted with the quartz reactor, collected using HRPD. The background shape is consistent with quartz and Bragg reflections are caused by steel.

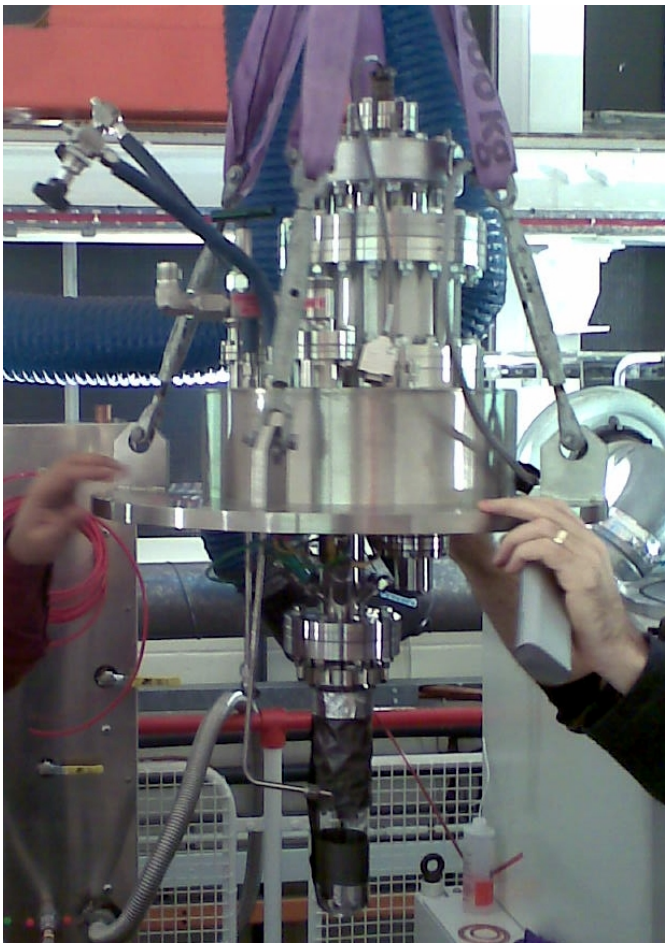

Figure 2.12: The IGA^{n} apparatus fitted with the quartz reactor and gadolinium foil neutron shielding in place.

2.12 Computational Methods

The use of computational techniques in modern science is undoubtedly important, even to an experimental Chemist! In this Thesis, computation is used primarily as a complimentary technique to aid in the analysis of diffraction and vibrational spectroscopy data, though it is also used to provide an added insight into molecular motion and the thermodynamic stability of various structures.

2.12.1 Density Functional Theory[87,88]

Density Functional Theory (DFT) started to gain popularity late 1960s following publication of seminal papers by Hohenberg and Kohn outlining its theory and Kohn and Sham implementing the theory.[89,90] Its basis lies first with the Born-Oppenheimer approximation, that it is possible to describe a solid system by the wavefunction of electrons in the presence of an external potential that is fixed and provided by the nuclei. This means that a many electron wavefunction describes the system, however it is not practically possible to solve this many body wavefunction. The first DFT theorem states that "the external potential $V_{ext}(\vec{r})$ is (to within a constant) a unique functional of $\rho(\vec{r})$; since, in turn $V_{ext}(\vec{r})$ fixes $\hat{H}$ we see that the full many particle ground state is a unique functional of $\rho(\vec{r})$." [89] (Where $\rho(\vec{r})$ is the electron density, and $\hat{H}$ is the Hamiltonian operator.) The ground state energy is a functional of the ground state electron density, so

$$E_0[\rho_0] = T[\rho_0] + E_{ee}[\rho_0] + E_{Ne}[\rho_0] \tag{2.25}$$

where T is the kinetic energy, E_{ee} is the electron electron potential and E_{Ne} is the nuclear electron potential. This means that the total energy of a system of electrons in an external potential is a unique functional of the groundstate density (Equation 2.26); if you find the density, then you can calculate the energy.

$$F_{HK}[\rho] = T[\rho] + E_{ee}[\rho] = \langle \Psi | \hat{T} + \hat{V}_{ee} | \Psi \rangle \tag{2.26}$$

Unfortunately, this functional ($F_{HK}[\rho]$) remains the unknown holy grail of DFT, but it is known that even relatively crude approximations can give excellent results. The ground state density uniquely determines the Hamiltonian operator, which characterises all states of the system, both ground and excited. Thus, all properties of all states are formally determined by the ground state density.

The second theorem states that $F_{HK}[\rho]$, the functional that delivers the ground state energy of the system, delivers the lowest energy if and only if the input density is the true ground state density, ρ_0.[i] This density is the exact single-particle ground-state density and Kohn and Sham were able to show that it is possible to replace the many-electron problem with an exactly equivalent set of solveable one-electron equations. This is a huge step forward except that there are still an infinite number of calculations to perform on an infinite number of electronic wavefunctions and an infinite basis set for each wave function.

At this point Bloch's theorem comes into play, it states that in a periodic cell each electronic wave function is the product of a cell-periodic part and a wavelike part (Equation 2.27). The cell part can be expanded using a basis set consisting of a discrete set of plane waves whose wave vectors are the reciprocal lattice vectors ($\mathbf{G}$) of the crystal, and each electronic wave function can be written as a sum of plane waves (Equation 2.28).

$$\Psi_{i,k}(\mathbf{r}) = exp[i\mathbf{k} \cdot \mathbf{r}] f_i(\mathbf{r}) \tag{2.27}$$

[i] So the energy obtained from the functional $E_0[\rho_0]$ is an upper bound to the true ground state energy, E_0, unless the exact ground state density is known.

$$\Psi_{i,k}(\mathbf{r}) = \sum_{G} c_{i,\mathbf{k}+\mathbf{G}} exp[i(\mathbf{k}+\mathbf{G})\cdot\mathbf{r}] \tag{2.28}$$

Bloch's theorem means that electronic states are allowed only at a set of **k** points determined by the boundary conditions of the bulk solid. Therefore an infinite number of electrons is accounted for by an infinite number of **k** points but with only a finite number of states at each **k** point. The problem of how to calculate this infinite number of wavefunctions is solved by the fact that **k** points that are very close together are very similar. Thus calculation at a single **k** point represents one area in **k** space and it is only necessary to perform a finite number of calculations. The electronic wave functions at each **k** point can be expanded in terms of a discrete plane-wave basis set. In principle an infinite plane-wave basis set is required to expand the electronic wave functions, however waves of lower kinetic energy are more important than higher energy, so the basis set can be truncated to include waves below a certain cut-off. The result is that by sampling a suitable number of **k** points (formally the sampling points for Brillouin zone integration) and selecting a suitable plane-wave cut-off energy, it is possible to solve the electronic wave functions and within DFT calculate a good approximation to E_{HK} and therefore all the properties of the system.

2.12.2 CASTEP Code[91,92]

CASTEP is a software package which uses density functional theory to provide a good atomic-level description of materials and molecules. It employs pseudopotentials, which replace the pure Coulomb potential of a positively charged nucleus with the combined electrostatic potential of the (positive) nucleus and the (negative) core electrons. Having this weaker potential makes solving the Schrödinger equation simpler. The program then attempts to minimise the total energy functional, E_{HK}.

Through the use of CASTEP, information can be gained about total energies, forces and stress in an atomic system. In addition optimum geometries, band structures, optical spectra, phonon spectra, molecular dynamics and so on may be calculated. In this Thesis four types of calculation were performed; single-point energy, geometry optimisation, phonon, and molecular dynamics. Before performing any of the latter three calculations it is desirable to perform checks to see if the selected plane wave cut-off energy and **k** point sampling will produce an accurate result. These checks may be performed on simple results of single-point energy calculations that are observed to converge to a limit when an appropriate **k** point sampling or plane wave cut-off energy is used. These simple results are *i*) the internal energy; *ii*) the atomic forces on any atom; and *iii*) the stress on the unit cell. These convergence tests are necessary for if the cut-off energy or **k** point sampling are set too high or too frequently respectively then valuable computation time may be wasted for little improvement in the quality of information gained. This process was performed for $Li(NH_3)BH_4$ and $Mg(NH_3)_6Cl_2$ for which data in Appendix A show that convergence was achieved using a **k** point sampling of 0.08 $Å^{-1}$ and a plane wave cut-off of 500 eV for both materials. These values were kept consistent for all $Li(NH_3)_nBH_4$ and $Mg(NH_3)_nX_2$ calculations due to the similarities of the materials and to add a level of consistency to the calculations.

Single-point Energy

Single-point energy calculations compute the energy of a particular, fixed, arrangement of atoms. These are used in calculating the convergence criteria, and are also useful in calculating relative energies of a specific molecular or structural orientation. The result of these calculations is the internal energy of the structure, that is the energy of the arrangement of atoms with respect to a reference state where all nuclei and electrons are infinitely separated from each other and at rest, this energy may be thought of as a 'quantum enthalpy of formation.'

Geometry Optimisation

Geometry optimisation calculations use an optimisation algorithm to compute a minimum energy state of the system within energy and atomic force criteria. Though a powerful technique, the force minimised structure is not necessarily the most stable nor does its calculation guarantee that it will ever exist in reality. The algorithm will simply find the nearest local energy minima, not the global minima, and thus must be treated with caution. Two different regimes were used; 'rough optimisations' which locate atoms to allow for atomic forces less than 0.05 meVÅ^{-1} which is deemed appropriate for structural information, and 'final optimisations' which locate atoms to allow for atomic forces less than 0.001 meVÅ^{-1} and are necessary for further phonon or molecular dynamics calculations.

Calculated bond lengths are rarely identical to those observed experimentally, and it should not be expected that they are. In the case where calculated bond lengths are shorter than those observed it may be due to the anharmonicity of the real system, calculations are carried out within the harmonic oscillator approximation and the anharmonicity of a real oscillating bond may result in longer bond lengths at higher temperatures as shown in Figure 2.13. A bending bond observed using diffraction or other averaging techniques may be seen as shorter than the same bond in a calculation. This is because when a moving or disordered atom is observed, the geometric average atomic position will be seen. If the atom is moving in an arc then the geometric average will be inside the radius of this arc and a shorter bond is observed, as shown in Figure 2.14.

The energy result of these calculations is used to calculate various enthalpies of reaction using Hess's Law. This is possible because the internal energy is related to the enthalpy as shown in Equation 2.29. Where reactions involve a change in the amount of gas present as well as a change in solid phases, the dV term may be approximated to dV_{gas} as the change in the solid volume is negligible. Another

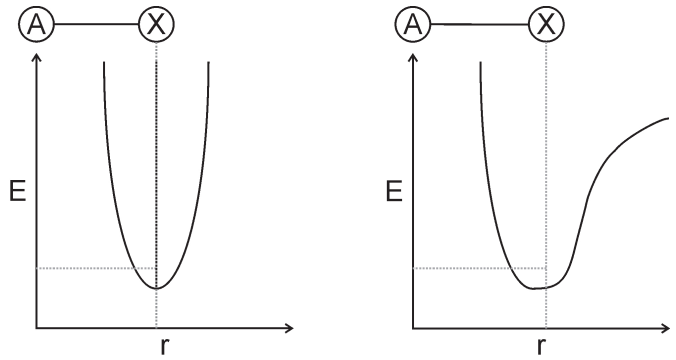

Figure 2.13: A sketch diagram to indicate how anharmonic bending or stretching bonds may appear longer in diffraction experiments (right) than in calculations (left).

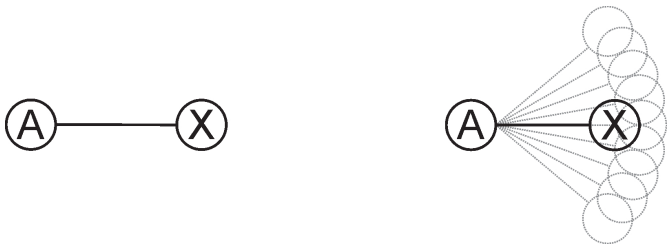

Figure 2.14: A sketch to indicate how bending bonds may appear shorter in diffraction experiments (right) than in calculations (left).

consideration is that the calculations do not include any zero-point energy so will contain an error of the order of a few kJmol^{-1}.

$$dU = dH + pdV \tag{2.29}$$

Phonon

Phonon-mode calculations give all the vibrational modes of a compound, including the eigenvalues and eigenvectors of each mode. The calculations are performed by perturbing the atomic positions and then expanding the total energy in a perturbation series, and may be used in a number of ways. In this Thesis, they are used to produce videos of the various vibrational modes, to assess the stability of calculated structures, to calculate INS and Raman spectra, and to calculate the mean squared displacement of atoms at various temperatures. Generally a structure is considered

unstable or, at least, worthy of closer inspection, if negative modes are calculated. A negative frequency mode implies a negative spring constant (k) in the description of a harmonic oscillator $E = \frac{1}{2}kx^2$ and thus a local maximum rather than minimum in energy. The consequences of this are shown in Figure 2.15(a-c). The Figure shows a) the situation for a positive value of k with the normal energy curve; b) the situation with a negative value of k resulting in a negatively sloping energy curve; and c) the reality of a negative value of k in which the energy levels would return to normal after some small displacement, resulting in a double-well potential. This is of course the most simple case, and each calculation of negative modes should be treated independently.

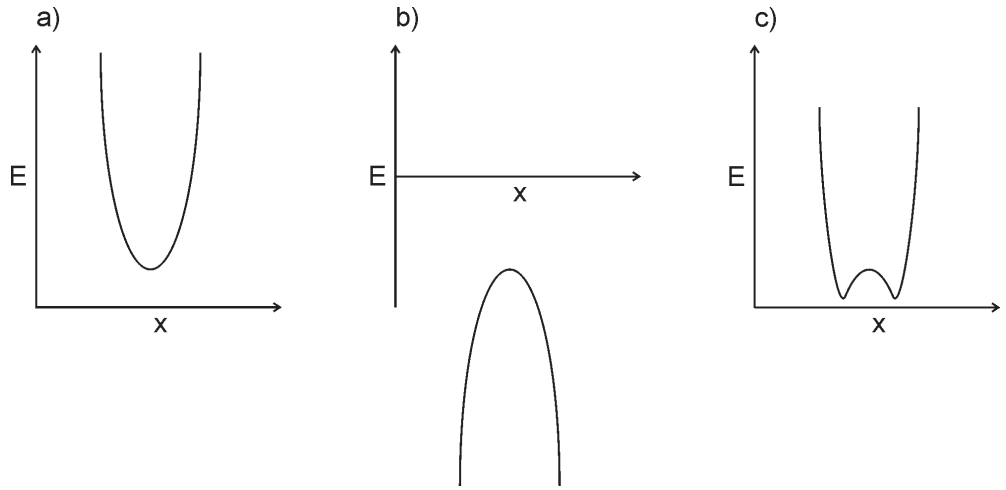

Figure 2.15: The energy curves $E = \frac{1}{2}kx^2$ for a) a positive value of k; b) a negative value of k; and c) a more realistic vision of a negative value of k.

With phonon mode data it is possible to calculate mean squared displacement of atoms at a given temperature. In the harmonic approximation, the displacement vectors of an atom, l, with a frequency, ω_v, at temperature, T may be calculated using the relationship:[80]

$$ {}^{v}\mathbf{B}_l =^{v} \mathbf{u}_l^2 \frac{16.9}{{}_{v}\mu\omega_v} \coth \frac{1.47\omega_v}{T} \tag{2.30} $$

The individual modes are orthogonal to one another and their displacements

follow a Gaussian probability distribution. Given the quadrature convolution properties of a Gaussian distribution, the total mean squared displacement of an atom at a given temperature may be calculated by summing the contributions of all the individual modes, thus:[80]

$$\mathbf{B}_l = \sum_{v}^{v} \mathbf{B}_l \tag{2.31}$$

This process was performed using a script written by Dr. Timmy Ramirez-Cuesta, and though important to consider any negative modes in these calculations it was found that their inclusion or rejection had little impact on the observed mean squared displacement of atoms.

Molecular Dynamics

Molecular dynamics (MD) calculations simulate the motion of atoms within a solid. Calculations were performed using the NVE ensemble in which initial velocities are assigned to atoms randomly such that the total linear momentum is zero and the temperature matches that specified (and calculated using the ideal gas thermometer shown in Equation 2.32). Calculations were performed using optimised structures at a MD temperature of 150 K, a time step of 0.5 ps was used following a 3.0-6.0 ps equilibration period in which the temperature was fixed. The NVE ensemble maintains a constant energy within the system, this was chosen as it allowed the simplest and most appropriate viewing of the molecular motion of atoms.

$$T = \frac{2}{3Nk_B} \sum_{i=1}^{N} \frac{m_i \|\mathbf{v_i}\|^2}{2} \tag{2.32}$$